Research Article

Numerical Investigation on the Thermal Protection Characteristics of a New Active Jet Design Parameter for Hypersonic Flight Vehicle

Songyan Tian ⓘ**, Yanhui Duan** ⓘ**, and Hongbo Chen** ⓘ

School of Systems Science and Engineering, Sun Yat-sen University, Guangzhou, China

Correspondence should be addressed to Hongbo Chen; chenhongbo@mail.sysu.edu.cn

This study investigated the thermal protection performance of an active jet thermal protection system (*PRs*AJ-TPS) based on a new jet design parameter *PRs* for hypersonic flight vehicles (HFVs). The new parameter *PRs* is defined as the relationship between the jet flow total pressure and the free flow total pressure behind the outer bow shock. A 20° tilted nozzle design is employed together with the *PRs* to form the *PRs*AJ-TPS. Theoretical and numerical analysis is performed to prove the advantages of using the *PRs*. A conventional in-house CFD solver with the *k-ω* SST turbulence model is utilized to perform the calculation. The influence of different *PRs* (working in the short penetration mode) and flight angles of attack on the performance of the *PRs*AJ-TPS is also studied. The simulation results confirmed that with a constant *PRs*, the Mach disk location stays the same and the normalized heat flux reduction is similar at different flight conditions. Nearly linear relationships exist between the new design parameter *PRs* and thermal protection performance indicators. The *PRs*AJ-TPS also exhibits good protection when flight angle of attack (AoA) varies between 0° and 40°, with the best results achieved at AoA = 0°. This study provides valuable information for the engineering application of the jet-based TPS to future HFVs.

1. Introduction

A safety threat accompanying hypersonic flight is the severe aerodynamic heating that could burn a thermally unprotected hypersonic flight vehicle (HFV) to ashes. Currently, most flight-tested HFVs employ passive TPS, whose performance is heavily based on the properties of the TPS materials. The passive TPS will either endure the extreme heating to a certain extent (e.g., TUFROC up to 2200 K, see [1]) or take away the heat through ablation. The passive TPS is simple and reliable, but also limits the performance and mission profile of the HFV by enforcing the constraint of material operating temperature. Since finding more capable materials for the passive TPS is extremely challenging, being also hardly reusable has eventually prevented the passive TPS from being the most competitive candidate for future TPS of reusable HFVs.

An alternative is the active TPS. By active, it means that additional energy input is needed to generate the desired thermal protection effect. Although active TPS is normally more complex due to the additional coolant supply system, they are easily reusable and could be powerful at certain locations with potential aerodynamic drag reduction effect. Active TPS in the context of external surface cooling of HFVs includes primarily energy deposition, transpiration cooling, opposing jet, and their combinations [2].

The energy deposition method uses electromagnetic energy to interrupt and displace the bow shock ahead of the nose cone or leading edge to achieve the thermal protection of the stagnation point and drag reduction. Laser and plasma actuators are among the most popular options (see [3–5]). Transpiration cooling mimics the natural cooling mechanism "sweating" of living beings. The TPS material is made porous, allowing the coolant to flow through it

and take away the heat. Recent progress in terms of the HFV external surface cooling could be referred to the SHEFEX II HFV and its flight test (see [6–8]).

Employing an opposing jet for thermal protection of the surface of high speed flight vehicles could be traced back to McMahon [9], who was inspired by the pioneering transpiration cooling research from Klunker and Ivey [10]. The author of [9] experimentally studied the transient flow field of an opposing jet on a blunt body and identified the cooling effect. A later experiment from Warren [11] confirmed the reduction in the heat transfer rate on the model surface and complemented McMahon's finding with steady-state measurement results. Finley [12], the author, studied the flow field of opposing jets both experimentally and analytically. His detailed study revealed most of the key relationships and physical characteristics of the opposing jet flow field. These early studies laid the foundation of subsequent opposing jet research.

In 2003, Hayashi and Aso [13] placed an opposing jet on the stagnation point of a sphere cylinder model with higher total pressure ratios than Warren [11]. A significant heat reduction effect was observed in supersonic free flow, and sufficient data were collected from this experiment. Their work was then widely used as the validation case for computational fluid dynamics (CFD) simulations involving opposing jets. On the other hand, the researcher concentrated on the long and short penetration mode of the opposing jet flow pattern [14]. The authors of [15] have a similar focus with experiments in Mach 6. Other experimental research also include [16–19].

Various numerical researches are equally available. Regarding the aspect of heat reduction, the authors of [20] analyzed the influence of jet total pressure on the shock standoff distance using the same opposing jet setup as in [13]. Research from [21–23] provide abundant information around the influence of jet nozzle shape and free flow incidence angle on the jet flow field and the subsequent heat reduction effect. In addition, [24] numerically validated their opposing jet on a waverider with variable blunt nose radii. The authors of [2] also analyzed the opposing jet penetration modes and the heat reduction effect with various jet total pressure ratios and exit Mach numbers. The authors of [25] considered the cavity effect of the off-working opposing jet. Research from [26] lays emphasis on the fluid-solid coupled method for the heat flux reduction effect. Another popular aspect of research is the drag reduction, which includes research from [27–30]. A sensitivity analysis is available from Guo et al. [31], which reveals that the total pressure ratio between the opposing jet and the free flow, the jet exit Mach number, and the free flow Mach number contribute to 92% of the change in model surface pressure, providing helpful guidance for the design of the opposing jet. Some other research had studied the opposing jet parametrically, such as [32–34]. The pieces of research mentioned above provide knowledge regarding the flow characteristics, parameter design, and simulation guidelines of the opposing jet.

A step forward is the category of the combined TPS based on the opposing jet, among which the aerospike serves as the main partner. Research from [35, 36] employed various combination of opposing jet with aerospike and aerodisk, and they also investigated the effect of using carbon dioxide and helium as coolant. The authors of [37–39] reported multiple research on the opposing jet and its combination with transpiration cooling. Zhang et al. [40] launched a transient numerical investigation on a design with a centered opposing jet and a circular slot around the centered jet. Paper [41] numerically compared the performance of the design from [40] with a single opposing jet in hypersonic nonequilibrium flow. Works from [42–50] all choose the option of combining the opposing jet with the aerospike. Some of them changed the jet into a lateral jet, while others used the opposing jet directly on the tip of the aerospike. Among them, Moradi et al. [45] and Pish et al. [46] investigated the cooling effect of various gases. Ou et al. [44] also found that the k-ω SST turbulence model performed better regarding the simulation of the opposing jet flow field. The authors of [51, 52] proposed and validated a design that combined an opposing jet, a lateral jet, and the aerospike altogether. The authors from [53] innovatively placed an additional jet on the back of an aerodome, which is on the tip of an Aerospike and has already an opposing jet. The additional rearward jet helps to reduce the peak heat flux on the spike and the main body caused by the flow reattachment.

Although many designs with good performance have been proposed, the scope of most research is still limited. Analysis and system designs are carried out mainly on the most severe aerodynamic heating scenario. This is 100% right for the passive TPS research, but is probably insufficient and inefficient for the practical application of the opposing jet on the full flight trajectory. Since setting a constant pressure or working state of the opposing jet throughout the whole flight trajectory does protect the HFV from the worst aerodynamic heating condition, it also wastes too much working fluid under other less severe conditions. The opposing jet is actually flexible and could be adjusted to the optimal and most efficient state depending on the flight condition. Yet few research have laid emphasis on how or according to what criteria the jet flow parameters should be regulated.

In the present study, an alternative solution to the question above, namely, the PRs based active jet thermal protection system (PRsAJ-TPS), has been proposed. The PRsAJ-TPS distinguishes itself from other opposing jets by adopting a new jet design parameter PRs, which is the total pressure ratio of the jet flow and the free flow behind the shock. The PRsAJ-TPS also takes a tilted jet nozzle design, aligning with the nominal angle of attack of the HFV trajectory.

The purpose of this work is to investigate the characteristics of the PRsAJ-TPS: (1) the ability of maintaining a similar thermal protection range and performance under quite different flight conditions, this characteristic is critical for an easier and more accurate evaluation of the total coolant consumption during flight mission design phase; (2) the relationship between PRs and protection performance, this information is helpful for the pre- and in-flight determination/adjustment of the PRs value; and (3) the protection stability of the PRsAJ-TPS against the variation of angle of

attack, this could guarantee the safety of the HFV during maneuver. Section 2 of this paper first introduces the theoretical basis of the new jet design parameter *PRs* and then illustrate the geometry of the demonstrative HFV model and boundary conditions. The comparative study method and a few customized thermal protection indicators are also explained in this section. The numerical method and its validation against the experimental results from [54] are presented in Section 3. The in-house CFD code utilized is Reynolds-averaged Navier-Stokes (RANS) equations based. The selected turbulence model is the $k\text{-}\omega$ SST model [55]. A grid independence study is presented in the end of this section. All computational results are then presented and analyzed for the three purposes in Section 4. The last section concludes the key findings of this work.

2. Theory and Methods

2.1. Introduction of the PRs. Most research on the active/opposing jet thermal protection method employ a straightforward total pressure ratio $PR = P_{j,0}/P_{f,0}$, a ratio between the jet flow total pressure (with subscript j) and the free flow total pressure (with subscript f), as the jet design parameter (whereas subscript 0 represents the total/stagnation value).

However, the author noticed in a pilot 2D sonic opposing jet research that a constant *PR* can neither be used to acquire a similar jet flow field nor the location of the shock structure under different flight conditions on a typical HFV flight trajectory. For each new free flow condition, several trial cases need to be computed to find a suitable *PR* value for a certain thermal protection range. When the flight condition deviates too much from the original free flow condition for jet design, using *PR* cannot even guarantee the proper functionality of the sonic nozzle. In fact, the choice of *PR* should first guarantee that the jet total pressure $P_{j,0}$ is larger than the free flow postshock stagnation point total pressure (also mentioned in [56]), yet the *PR* does not intrinsically include this critical requirement. Therefore, problems arise easily when flight conditions change. The analysis is as follows.

The ratio σ_s between the flow total pressure behind a normal shock $P_{s,0}$ and the free flow total pressure $P_{f,0}$ is given using the normal shock relation. The value $P_{s,0}$ is taken as a reasonable estimation of the actual free flow total pressure behind the outer bow shock.

$$\sigma_s = \frac{P_{s,0}}{P_{f,0}} = \frac{\left[(\gamma+1)Ma_f^2/2 + (\gamma-1)Ma_f^2\right]^{\gamma/(\gamma-1)}}{\left[(2\gamma/(\gamma+1))Ma_f^2 - ((\gamma-1)/(\gamma+1))\right]^{1/(\gamma-1)}}. \tag{1}$$

The σ_s increases monotonically with a decreasing free flow Mach number, as shown in Figure 1(a). It means that as the flight Mach number drops, the $P_{s,0}$ behind the shock tends to converge to the $P_{f,0}$ in the far field. From the colored contours in Figure 1(b), the convergence of the two parameters is apparent at low Mach numbers.

For a typical HFV trajectory, the flight Mach number does decrease as the altitude drops. In the case of an opposing jet designed for a higher altitude, the opposing jet will not function well at low altitudes unless adjustment is made. In contrast, if one designs the opposing jet at a lower altitude, the opposing jet will be overly sufficient when operating at high altitudes, wasting too much working fluid.

For instance, the $P_{j,0} = PR \cdot P_{f,0}$ with $PR = 0.00215$ is designed for the flight condition of altitude 70 km and Mach 25 (shown in Figure 1(b)). The greyscale contour surface of $P_{j,0}$ clearly intersects with the colored contour surface of $P_{s,0}$ at around $Ma = 10$ for all flight altitudes. Meaning that the jet will cease to function for the HFV flight conditions with Mach number less than 10. Without changing the value of *PR* along the trajectory, the opposing jet will lose its thermal protection effect.

One might argue that choosing a large enough *PR* could solve the problem and cover all flight conditions, yet the resulting enormous and excessive amount of coolant demand will simply deny this solution. It could also be argued that the *PR* is not necessary to remain constant. However, the problem is that there is now not much guidance on how to set a suitable *PR* for new flight conditions without any CFD trial cases. Finding a new parameter which is available once and for all flight conditions is thus necessary to enable the actual application of the opposing jet base active TPS.

Here in this study, a new total pressure ratio *PRs* is proposed as a key parameter for jet flow design. With a proper selection of the *PRs*, the designed working state of the *PRs*AJ-TPS nozzle will be economically ensured throughout the trajectory. Depicted in Figure 1(b) is an example of $PRs = 60$, corresponding to $PR = 0.00215$ for the flight condition of altitude 70 km and Mach 25. It is apparent that the new greyscale contour surface of the *PRs* based jet total pressure $P_{j,0,N} = PRs \cdot P_{s,0}$ always runs over the contour surface of $P_{s,0}$ equidistantly. This is the first advantage of the *PRs*.

The second advantage of the *PRs* is that a constant *PRs* could also maintain a similar shock structure of the jet flow field under quite different flight conditions. The concept of a virtual supersonic nozzle could be used to explain such characteristics of the *PRs*. A typical jet flow field is depicted in Figure 2. Here, the jet nozzle of the *PRs*AJ-TPS is assumed to be sonic.

Distinguished from the hypersonic flow field with no active jet (refer to [54]), three more characteristic structures appear in the jet flow field: the contact surface, the Mach disk, and the barrel shock. The jet flow exiting from the nozzle normally has high pressure. Therefore, it goes through an intensive expansion process encapsulated by the Mach disk and the barrel shock. Due to different flow properties, a contact surface is also formed after the jet flow meets the free flow.

From the continuum assumption of fluids, the total pressure of the jet flow should be equal to the free flow total pressure behind the outer bow shock $P_{s,0}$ at some point. The jet flow total pressure $P_{j,0}$ is much higher than the $P_{s,0}$, as the *PRs* is much larger than one. And the free flow total pressure loss through the inevitable outer bow shock cannot be replenished without any external work on it. Thus, it is the jet flow that needs to dissipate its energy through the irreversible process of shock
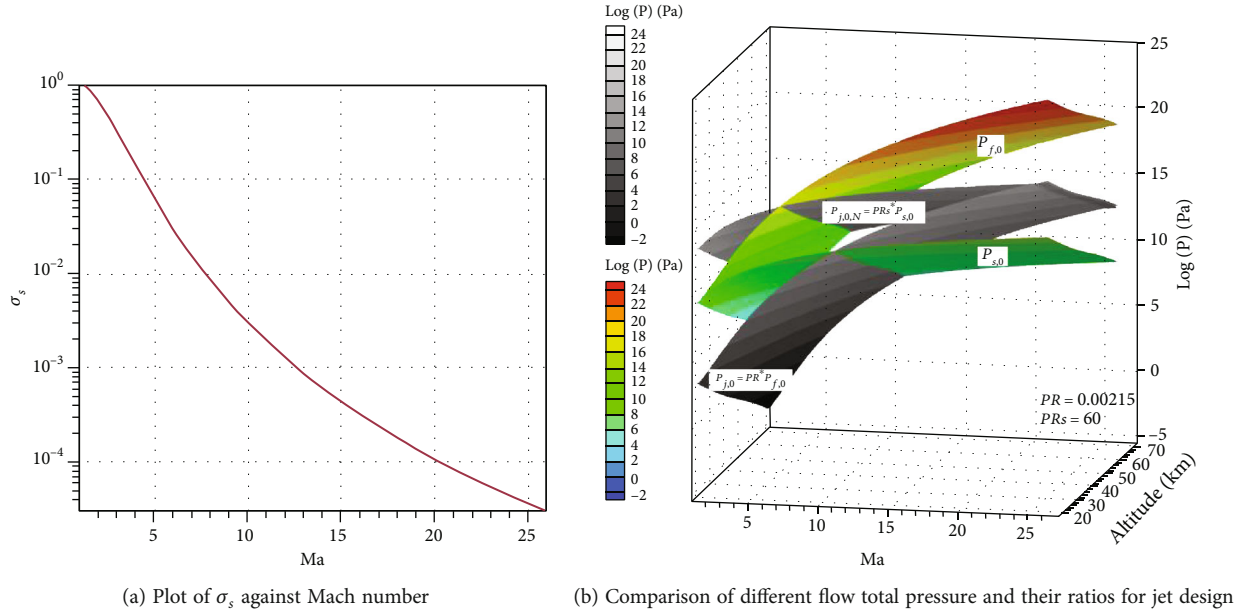
(a) Plot of σ_s against Mach number

(b) Comparison of different flow total pressure and their ratios for jet design

FIGURE 1: Plot of the total pressure ratio σ_s versus the Mach number and comparison between different total pressure ratio.
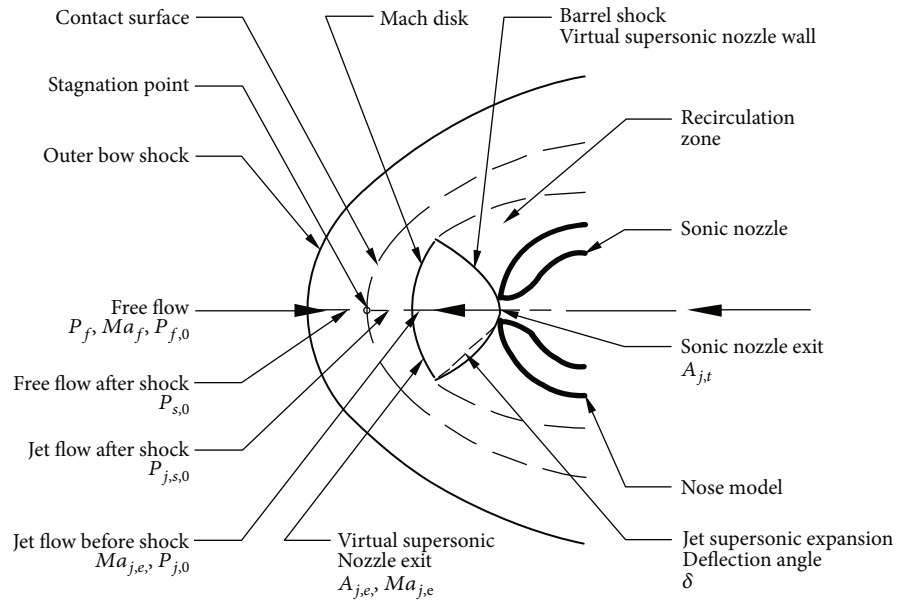

FIGURE 2: Concept of the virtual supersonic nozzle.

compression, in order to reach an equilibrium with the free flow behind the shock. The Mach disk is then formed after the initial jet expansion. Analyzing the jet along the center line, the jet total pressure $P_{j,s,0}$ after the Mach disk is solely determined by its Mach number $Ma_{j,e}$ before the shock. There is then:

$$P_{j,s,0} = P_{j,0} \cdot \sigma_{j,e}\left(Ma_{j,e}\right) = PRs \cdot P_{s,0} \cdot \sigma_{j,e}\left(Ma_{j,e}\right), \quad (2)$$

$$\frac{P_{j,s,0}}{P_{s,0}} = PRs \cdot \sigma_{j,e}\left(Ma_{j,e}\right) = 1. \quad (3)$$

As the $P_{j,s,0} = P_{s,0}$ after the Mach disk, $\sigma_{j,e}(Ma_{j,e}) = 1/(PRs)$. Therefore, $\sigma_{j,e}(Ma_{j,e})$ or precisely the $Ma_{j,e}$ is related only to the constant PRs. A similar relation is statistically fitted by [57] for under underexpanded jet in quiescent medium. Yet, the physical mechanism is not explained, and the opposing jet flow field shows difference in hypersonic flow.

Now consider such a process from another perspective. The Mach disk could be viewed as a normal shock covering the exit of a supersonic nozzle, the same as [12] assumed in his paper. Then, the $P_{s,0}$ is exactly the total backpressure of a supersonic nozzle when a normal shock appears exactly at the exit plane.

As $\sigma_{j,e}(Ma_{j,e})$ has already been determined by the constant PRs, $Ma_{j,e}$ is then known. The $Ma_{j,e}$ could also be viewed as the exit Mach number of the supersonic nozzle. There is then:

$$\varepsilon = \frac{A_{j,e}}{A_{j,t}} = \frac{1}{Ma_{j,e}} \left[\left(1 + \frac{\gamma - 1}{2} Ma_{j,e}^2 \right) \frac{2}{\gamma + 1} \right]^{(\gamma+1)/2(\gamma-1)}, \quad (4)$$

i.e., $Ma_{j,e}$ produces a fixed area expansion ratio $\varepsilon = A_{j,e}/A_{j,t}$, where $A_{j,e}$ is the exit plane area of the virtual supersonic nozzle. Considering the virtual supersonic nozzle, the Mach number at the throat is always 1 at different flight altitudes since the actual jet nozzle is a sonic one.

According to the Prandtl-Meyer expansion, the deflection angle of the jet leaving the actual sonic nozzle could be obtained by:

$$\delta = v(Ma_{j,e}) - v(Ma_j) = v(Ma_{j,e}), \quad (5)$$

whereas $v(Ma)$ is the Prandtl-Meyer function, with $v(Ma_j) = 0$ for $Ma_j = 1$. This means the assumed virtual supersonic nozzle expansion section has an approximate cone half-angle δ defined only by $Ma_{j,e}$. As it has been proved that at different flight conditions the $Ma_{j,e}$ is constant, there is thus an identical virtual supersonic nozzle. The area expansion ratio ε and the resulting $A_{j,e}$ for the Mach disk plane also remain the same. The axial location of the Mach disk plane with respect to the nozzle throat is then fixed. Finally, remember that the $Ma_{j,e}$ is given by the selected constant PRs, and the virtual supersonic nozzle and the Mach disk location are proved to be strongly related to the PRs.

Since the locations of the main flow structures, such as the Mach disk, have a significant influence on the thermal protection intensity and range of the jet, being able to ensure a similar Mach disk location at different flight conditions makes the PRs a more convenient jet design parameter.

2.2. Model Geometry. The geometric model being investigated is a nose section of a wing-body HFV. The head of the nose is spherical with a radius of 0.015 m. The model is symmetric against both the xoy (vertical central plane) and the xoz (horizontal central) plane as shown in Figure 3. The model has a total length of 0.400 m, and its maximum wingspan reaches 0.267 m. The maximum thickness of the HFV model is 0.084 m. The model also has a wing sweep angle of 73°. A sonic nozzle is located at the tip of the nose with an exit radius of 0.002 m. As the nominal angle of attack (AoA) of the HFV is 20°, the nozzle is placed with its central axis rotating 20° around the z-axis, going exactly through the actual stagnation point during flight.

The computational gird of the HFV nose model is displayed in Figure 4. Taking the benefit of the symmetric configuration, only half of the 3D model is considered. The total number of cells is around 1.7 million, with the height of the first mesh layer being 0.001 mm ([24, 43, 54, 58]).

2.3. Boundary Conditions. There are four types of boundary conditions involved in the computation. The free flow condition is given by the primitive parameters: pressure P, temperature T, velocity V, turbulent kinetic energy k, and the specific rate of dissipation ω. The model wall is set to be 295 K isothermal for all computational conditions with the no-slip wall condition assumed. The outlet of the computational domain is set to be the supersonic outflow condition. The nozzle of the PRsAJ-TPS is characterized by the sonic flow condition using static parameters P and T.

The free flow parameters are obtained from the "U.S. Standard Atmosphere 1976" with altitudes and Mach numbers. The case label provides information about the flight altitude and Mach number through the formulation of "H#Ma#", e.g., H70Ma20 represents an altitude of 70 km and Mach number 20.

As for the PRsAJ-TPS nozzle, the nozzle exit plane parameters could be determined through the following relations with a given PRs:

$$\frac{P_j}{P_{j,0}} = \frac{P_j}{PRs \bullet P_{s,0}} = \left(1 + \frac{(\gamma - 1)}{2} Ma_j^2 \right)^{-\gamma/(\gamma-1)}, \quad (6)$$

$$\frac{T_j}{T_{j,0}} = \left(1 + \frac{(\gamma - 1)}{2} Ma_j^2 \right)^{-1}, \quad (7)$$

where $P_{s,0}$ could be calculated from equation (1). The relations above are derived under the isentropic expansion assumption within the nozzle. The nozzle jet total temperature $T_{j,0}$ is set to 300 K, and the T_j is thus 250 K. The free flow total pressure $P_{f,0}$ could be obtained similarly with equation (6).

For the assessment of the mass flow rate, the following equations could be used.

$$\dot{m}_j = K \frac{P_{j,0}}{\sqrt{T_{j,0}}} A_j, \quad (8)$$

$$K = \sqrt{\frac{\gamma}{R} \left(\frac{2}{\gamma + 1} \right)^{(\gamma+1)/(\gamma-1)}}. \quad (9)$$

With a given HFV trajectory, the total consumption working fluid could be estimated by integrating equation (8) over time. The equations above stand only if the jet flow could actually reach the sonic speed at the exit plane. To assess and guarantee this could really be achieved, free flow static pressure P_s behind the bow shock should be calculated and compared. This could be done with the normal shock relation.

$$P_s = P_f \left(\frac{2\gamma}{\gamma + 1} Ma_f^2 - \frac{\gamma - 1}{\gamma + 1} \right). \quad (10)$$

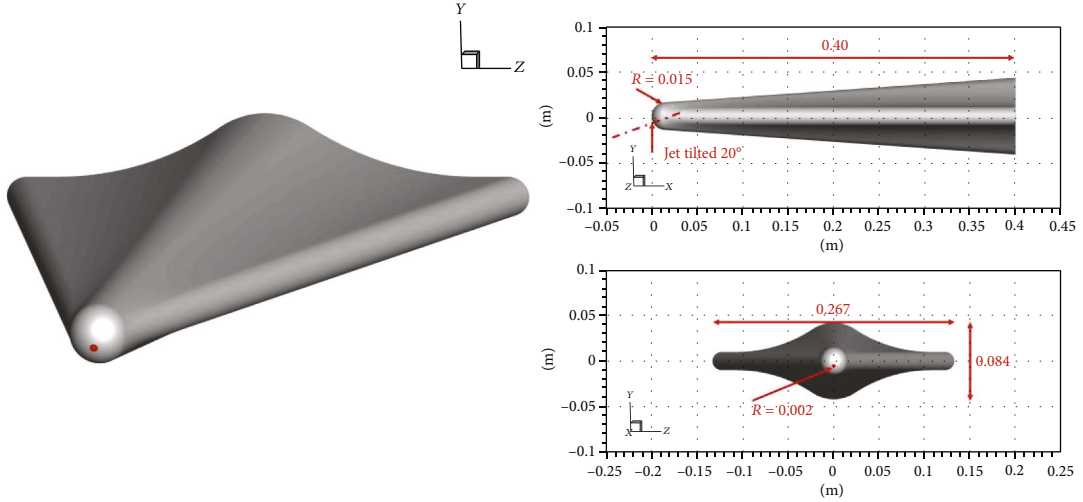With $P_s < P_j$, sonic speed will be reached at the exit plane. Alternatively, PRs could also be used to guarantee
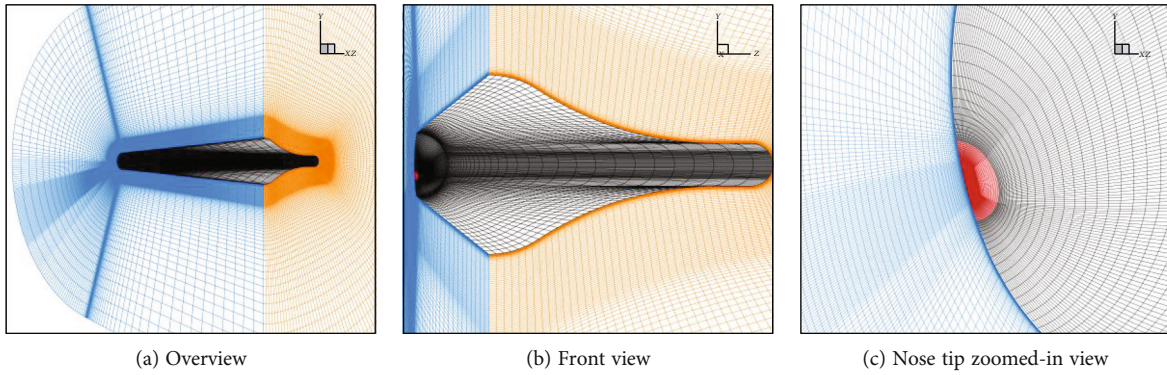
FIGURE 3: Geometry and dimensions of the model.

(a) Overview

(b) Front view

(c) Nose tip zoomed-in view

FIGURE 4: Computational grid (blue: symmetry plane; black: wall; orange: outlet; red: jet inlet).

such supercritical working condition of the nozzle more conveniently and conservatively. To find out the minimum allowed *PRs*, the following analysis applies:

$$PRs = \frac{P_{j,0}}{P_{s,0}} = \frac{P_j}{P_{s,0}}\left(1 + \frac{(\gamma - 1)}{2}Ma_j^2\right)^{\gamma/(\gamma - 1)}, \quad (11)$$

$$\frac{P_j}{P_{s,0}} = PRs\left(1 + \frac{(\gamma - 1)}{2}Ma_j^2\right)^{-\gamma/(\gamma - 1)}. \quad (12)$$

If P_j is larger than $P_{s,0}$, the sonic nozzle could also have $Ma_j = 1$. Therefore,

$$PRs > \frac{1}{\left(1 + ((\gamma - 1)/2)Ma_j^2\right)^{-\gamma/(\gamma - 1)}} = \left(\frac{\gamma + 1}{2}\right)^{\gamma/(\gamma - 1)}. \quad (13)$$

When the working fluid is air, i.e., $\gamma = 1.4$; then, *PRs* > 1.9. Thus, choosing a *PRs* greater than 1.9 will always have the sonic nozzle working properly.

2.4. Comparative Study Method. A comparative study method is used. An HFV trajectory with a 20° nominal angle of attack is selected. Four typical flight conditions ranging from altitude 70 km Mach 20 to altitude 40 km Mach 5 are investigated. For each of these four flight conditions, at least two cases are computed, one with the *PRs*AJ-TPS turned-off and one with it on. The influence of different *PRs* values and AoAs on the performance of the *PRs*AJ-TPS are studied at chosen flight conditions. Totally, 20 computational cases have been conducted, which provide information for the three aspects of interest regarding the *PRs*AJ-TPS:

(1) Performance of *PRs*AJ-TPS along a trajectory designed with the new parameter *PRs*

The selected four typical flight conditions from the trajectory are H70Ma20, H60Ma15, H50Ma10, and H40Ma5 (refer to Section 2.3 for label meaning). These cases have quite different free flow conditions. Such a situation poses difficulty for jets designed using the *PR* ratio, as it is difficult to achieve similar protection performance using PR. On the contrary, this problem could be easily dealt with by employing *PRs*. Using *PRs* as the key jet design parameter, the flow field characteristics of these flight conditions are thoroughly investigated and the advantages of *PRs* are numerically verified. Cases with the *PRs*AJ-TPS turned off all have the AoA = 20° and have the case label suffix "NJ." The cases with the suffix "NJ" provide the reference values of peak/

stagnation heat flux without any thermal protection at each flight condition. Cases with the *PRs*AJ-TPS turned on have the case label suffix "J." The standard condition of *PRs* = 60 and AoA = 20° is valid for these suffix "J" cases. Cases with the suffix "J" offer the results of the standard *PRs*AJ-TPS setting.

(2) Influence of different *PRs* values on the *PRs*AJ-TPS performance

The flight condition of altitude 50 km and Mach 10 is selected to investigate the influence of different *PRs*. The *PRs* values are 5, 15, 30, 45, and 60. This case series reveals the relationship of the *PRs*AJ-TPS thermal protection performance to the *PRs*. The reference peak heat flux without the *PRs*AJ-TPS has been obtained from the H50Ma10-NJ case. The case label suffix "Jet#" represents the *PRs* ratio used in the case with *PRs* = #.

(3) Influence of different flight angles of attack on the *PRs*AJ-TPS performance

In the real world, the HFV may have multiple angles of attack along its trajectory during flight. It is necessary and beneficial to examine the thermal protection performance of the nozzle tilted *PRs*AJ-TPS under various AoAs. The H70Ma20 and H40Ma5 series are selected as they are the two ends of the chosen trajectory. The *PRs* is still 60 for all *PRs*AJ-TPS turned on cases. The AoAs considered a range from 0° to 40° with an interval of 10°. The reference peak heat flux is taken from the corresponding suffix "NJ" case. The case label suffix "AoA#" represents the AoA used in the case with AoA = #°.

Comparative relations between cases are illustrated in Figure 5 below. The corresponding boundary conditions are summarized below in Table 1.

Several nondimensional indicators are taken to compare the thermal protection performance in each case: normalized surface heat flux $\dot{Q}N$, normalized length $x_{\dot{Q}N_{\max}}/l$, and $x_{\dot{Q}N=0.1}/l$.

The $\dot{Q}N$ indicator is used to quantify the surface heat flux across various case series:

$$\dot{Q}N = \frac{\dot{Q}}{\dot{Q}_{\max}}. \tag{14}$$

Here, $\dot{Q}N_{\max}$ is the peak/stagnation point heat flux of the corresponding label suffix "NJ" case. With $\dot{Q}N$, the thermal protection intensity from different case series is transformed into the same scale and could be easily compared.

Meanwhile, $x_{\dot{Q}N_{\max}}/l$ gives the normalized location of the maximum $\dot{Q}N$, and $x_{\dot{Q}N=0.1}/l$ offers the location of $\dot{Q}N = 0.1$. These two parameters are nondimensionalized with respect to the body length l and are used as indicators for the thermal protection range.

3. Numerical Method and Validation

3.1. Numerical Method. The in-house CFD code employed in this study for the hypersonic flow field analysis is conven-

tional and robust. The flow physics is characterized by the Reynolds-averaged Navier-Stokes equations in integral form under the conservative cell-centered finite-volume framework. For the spatial discretization, cell-centroid value-based multidimensional polynomials with total variation diminishing (TVD) [59] limiter are applied to reconstruct the conservative variables at cell face centroids. With two TVD limited inviscid flux computed from different polynomials from the two cells of a shared cell face, an approximate Riemann solver then deals with the interface wave propagation problem for the inviscid flux. Viscous fluxes are evaluated using the same base polynomials (yet without the TVD limiter) and are then averaged at cell interface. Since all the fluxes are known, a point-implicit time stepping scheme is used and the Gauss-Seidel scheme performs the update of the variables. The k-ω SST turbulence model is implemented, which is employed by a fair number of research regarding opposing jets ([2, 21–24, 31, 37–39, 43, 44, 47, 54]). Air is taken to be the flow medium and is characterized by the perfect gas law.

3.2. Validation Case. The numerical method is validated against the experimental results from [13], which is widely used as the validation case for the opposing jet related aerodynamic heat calculation. The geometric parameters are in accordance with the experiment. The computational model is simplified in the same way as [54] did. The grid for the validation case is shown below in Figure 6.

Experimental results for the NoJet and $PR = 0.6$ case are chosen for the validation. The free flow and jet flow are both air and their conditions are listed in Table 2.

The Stanton number St defined below is used to analyze the surface heat transfer effect [13]:

$$\dot{Q} = -\kappa \frac{dT}{dx_n} = -\kappa \frac{T_c - T_{\text{wall}}}{\Delta x_n}, \tag{15}$$

$$St = \frac{\dot{Q}}{\rho_f c_{p_f} u_f (T_{aw} - T_{\text{wall}})}, \tag{16}$$

$$T_{aw} = \left[1 + \sqrt[3]{\text{Pr}_w}\left(\frac{\gamma - 1}{2}\right)Ma_f^2\right]. \tag{17}$$

With $\dot{Q}N$ being the original surface heat flux computed by the CFD solver, the subscript n is the normal direction of the wall, Δx_n is the height of the first mesh layer, T_c represents the cell center temperature in the first mesh layer, and T_{wall} stands for wall temperature. The subscript f indicates the free flow, c_p is the specific heat capacity under constant pressure, T_{aw} is the recovery temperature of the adiabatic wall, and $\text{Pr}_w = 0.71$ is the wall Prandtl number from [13].

For the NoJet case, the results from the laminar and k-ω SST models are compared. For the $PR = 0.6$ case, only the result from the k-ω SST model is shown. The validation cases are listed in Table 3.

The laminar formulation predicts the NoJet case stagnation point heat transfer rate well, but fails to achieve an

Case series		Suffix					Notes
H70Ma20	NJ	J/AoA20	AoA0	AoA10	AoA30	AoA40	AoA investigation
H60Ma15	NJ	J					
H50Ma10	NJ	J/Jet60	Jet5	Jet15	Jet30	Jet45	*PRs* investigation
H40Ma5	NJ	J/AoA20	AoA0	AoA10	AoA30	AoA40	AoA investigation
	Reference cases without *PRs* AJ-TPS	Reference cases with *PRs* AJ-TPS					

FIGURE 5: Comparative case design and notes.

TABLE 1: Summary of boundary conditions.

| Boundary	Parameter	Value
Free flow	P_f	5.220 Pa (H70Ma20)
		21.955 Pa (H60Ma15)
		79.772 Pa (H50Ma10)
		287.125 Pa (H40Ma5)
	T_f	219.581 K (H70Ma20)
		247.018 K (H60Ma15)
		270.650 K (H50Ma10)
		250.351 K (H40Ma5)
	V_f	5941.25 m/s (H70Ma20)
		4726.13 m/s (H60Ma15)
		3298.03 m/s (H50Ma10)
		1585.97 m/s (H40Ma5)
Jet flow	P_j	*Calculate per case with equation (6) according to Figure 5.
	T_j	250.00 K (identical for all cases)
	Ma	1 (identical for all cases)
Model	T_W	295.00 K (identical for all cases)
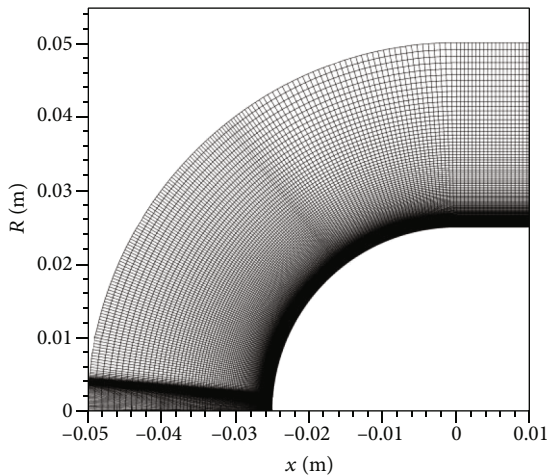
FIGURE 6: Gird of the geometry model for the validation case with dimensions.

accurate distribution of St over the whole model, as can be seen in Figure 7. Computational results using the k-ω SST model fit the experimental results well after $\theta > 20°$. Hayashi

and Aso [13] also mentioned the cause of such discrepancy: the laminar-turbulent transition occurred within $\theta < 20°$. For the $PR = 0.6$ case, the k-ω SST model works well.

Hence, for all cases investigated in this study, the k-ω SST model is selected.

3.3. Grid Independence. A grid independence study is performed to rule out the influence of the specific grid cell quantity. A fine grid with 2.0 million cells and a coarse grid with 1.4 million cells are used for the comparison. The grid with 1.7 million cells (Figure 4) is referred to as the moderate grid in this context. Since both the surface heat flux and the jet flow structure are of interest, the meshes differ from each other not only by the height of first layer of cells but also the number of layers normal to the model surface. They are illustrated in Figure 8. The boundary conditions of the case H60Ma15-J are employed for the calculation.

Figure 9 plots the heat flux $\dot{Q}$ results along the center line of the model windward surface. The pattern of $\dot{Q}$ distribution is identical for all three levels of grid. And there is no significant difference among the exact $\dot{Q}$ values from different grids, though the result from coarse grid deviates more from that of the fine grid. Considering the accuracy and

TABLE 2: Boundary conditions for validation.

Boundary	Parameter	Value
Free flow	P_f	9.709 kPa
	T_f	95.25 K
	V_f	778.862 m/s
Jet flow	P_j	434.247 kPa
	T_j	250.00 K
	Ma	1
Model	T_W	295.00 K

TABLE 3: Cases for validation.

Case	Turbulence model	Jet condition
1	Laminar	NoJet
2	k-ω SST	NoJet
3	k-ω SST	$PR = 0.6$
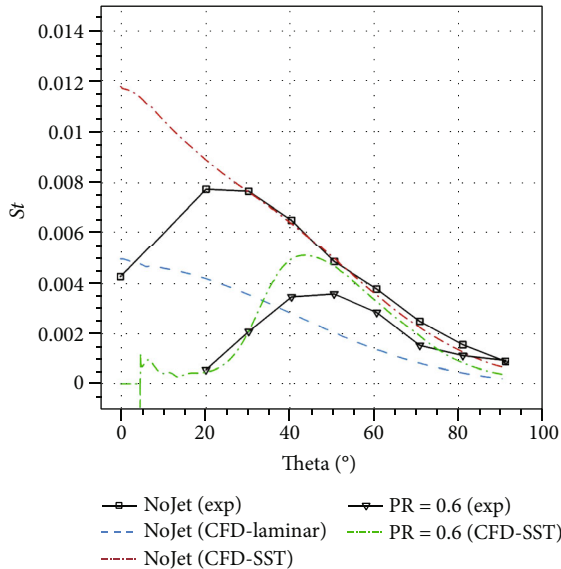
FIGURE 7: Validation results.

computational efficiency, the moderate grid with 1.7 million cells is the final choice for this study.

4. Results and Discussion

4.1. Overview of All Results. Figure 10 gives the streamlines of a typical flow field with the *PRs*-based active jet (case 4, H70Ma20-J), whereas coordinates *s* and *n* represent the normal and lateral distance to the center of the nozzle exit, respectively. The contour lines stand for the Mach number. Suggested from the curved outer bow shock and the Mach disk, the jet reached the typical short penetration mode (SPM). It can be seen that the active jet flows out of the

nozzle and goes through an intense expansion process forming an expansion fan, which is enclosed by the barrel shock. Out of the barrel shock, the recirculation region can be identified. A highly curved Mach disk then decelerates the main jet flow. After this, a stagnation point is formed ahead of the Mach disk. Starting from the stagnation point, the jet flow and free flow confront each other, resulting in a shear layer due to different flow properties. The flow field structure fits well with the virtual supersonic nozzle concept in Figure 2. The jet flow is initially bounded by the barrel shock, as it crosses the Mach disk and gets compressed, the flow close to the virtual wall changes direction immediately. A small fraction of it is then separated near the wall and flows back to the jet exit with high pressure, thus strengthens the barrel shock.

Different from similar studies with larger nose radii and relative lower jet total pressure, the jet expansion region outmatches the nose in size here. The recirculation zones with low temperature jet flow fill the gap between the expansion region and the nose, leaving the returned jet flow as well as the incoming free flow with no chance to impinge on the spherical nose achieving both heat flux and drag force reduction. The flows are forced to reattach the model surface tangentially, delivering a less turbulent boundary layer with reduced convective heat transfer intensity.

Table 4 summarizes the results of key thermal protection indicators for all cases. In the "NJ" cases, the maximum heat flux usually appears at the stagnation point. In the cases with the *PRs*AJ-TPS turned on, it is to be found on the leading edge.

Although the Stanton number is used in some literature to analyze heat flux, in the case of comparison across different flight conditions, $\dot{Q}N$ will be a better choice.

A few quick facts are listed here:

(i) The peak surface heat flux $\dot{Q}_{max}$ in "NJ" cases decreases as the altitude drops

(ii) With *PRs*AJ-TPS in operation, the $\dot{Q}_{max}$ drops substantially

(iii) In case 2 (H70Ma20-AoA0), the $\dot{Q}N_{max}$ reaches the minimum level of around 9% among all cases investigated; in contrast, maximum $\dot{Q}N_{max}$ appears in case 20 (H40Ma5-AoA40)

(iv) A constant *PRs* ratio provides a generally similar level of thermal protection at the same angle of attack, and the $\dot{Q}N_{max}$ stays around 0.28 with a standard deviation of 13%

(v) As the angle of attack or *PRs* ratio decreases, the model surface peak heat flux drops and the protection range increases

Detailed analysis will be given in the following sections.

4.2. Performance of the PRsAJ-TPS at Different Flight Conditions. Observing the suffix "NJ" and "J" cases at different altitudes, it can be noticed that the *PRs*AJ-TPS reduced the maximum heat flux on the model surface by at least

(a) Coarse mesh   (b) Moderate mesh   (c) Fine mesh
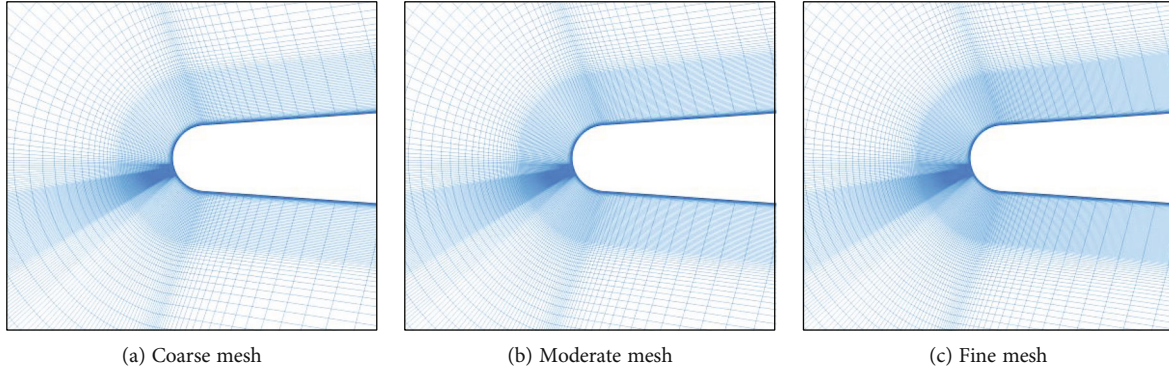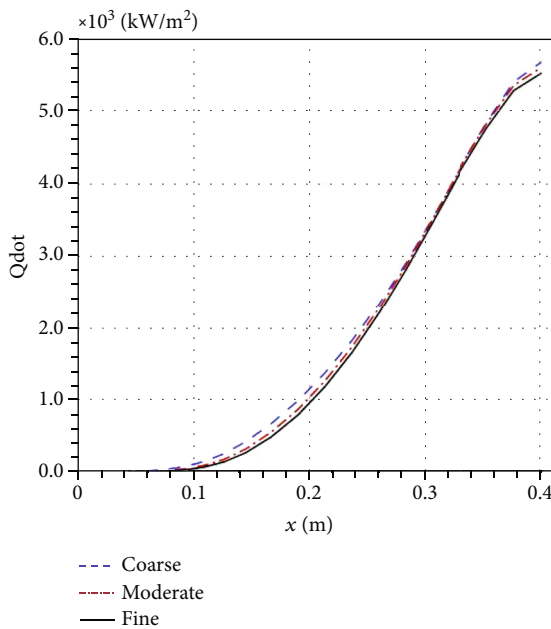
FIGURE 8: Side view of meshes with different density.

FIGURE 9: Results of $\dot{Q}$ distribution on the model windward surface center line from different grids.

68% (Table 3). The maximum heat flux in the H70Ma20 series drops from 3,691 kW/m^2 ("NJ" case) to 960 kW/m^2 ("J" case), which is a 74% reduction. The peak heat flux reduction is around 70% in the H60Ma15 series, while it is roughly 68% for the H50Ma10 series. In the H40Ma5 series, the reduction is 75%. With the PRs being 60, the resulting $\dot{Q}N_{max}$ values at different flight conditions reach an average value of 28.1% with a 2.9% standard deviation, compared with the corresponding "NJ" cases.

Figure 11 plots the $\dot{Q}N$ value of the "NJ" and "J" cases from different heights at every mesh point on the nose model in the x-direction. As can be seen from the figure, the "NJ" and "J" cases exhibit similar distributions of the $\dot{Q}N$, respectively. In each of the "NJ" cases, $\dot{Q}N_{max} = 1$, and it appears on the nose tip. A smaller peak, which originates from the reattachment of the free flow on the model, is visible at around $x = 0.08$ m on the leading edge.

The only peak of the $\dot{Q}N$ in each "J" case appears on the leading-edge, and it moves further backward from the nose tip as the altitude and Mach number increase. For instance, the location of the peak heat flux moved from $x_{\dot{Q}N_{max}}/l = 0.3\%$ (i.e., stagnation point) to 94.1% ($x = 0.377$ m, i.e., somewhere on the leading-edge) in the H70Ma20-J case. Taking a heat flux reduction of 90% (i.e., $\dot{Q}N = 0.1$) as a second protection indicator; then, about $x_{\dot{Q}N=0.1}/l = 58.2\%$ of the body will be under intense protection. Similarly, $x_{\dot{Q}N_{max}}/l$ is increased to 82.4% and $x_{\dot{Q}N=0.1}/l$ to 35.6% in the H40Ma5-J case.

From the streamlines in Figure 12, it can be observed that after the jet turns away from the original direction and flows back to the model, a shear layer between the reversed jet flow and the free flow forms. Since the free flow Mach number decreases as the HFV approaches the ground, the outer bow shock strength is weakened, and the free flow energy is less exhausted after going through the shock. The streamlines of the reversed jet flow are thus pushed further toward the model body at lower altitudes, resulting in an earlier appearing peak heat flux and a shorter protection range.

When comparing the flow field contour at different altitudes, it is clear that the shock standoff distances are visually identical. Figure 13(a) below plots the contour lines of the Mach number for the H70Ma20-J case. Figure 13(b) plots the total pressure coefficient c_{p0} and offers a closer examination of what happened to the jet as it develops.

The total pressure coefficient c_{p0} is the total pressure P_0 at every location in the flow field normalized against the jet total pressure $P_{j,0}$. Noticeably, the c_{p0} from different altitudes agreed with each other well from position $s = 0$ m to around $s = -0.04$ m. The c_{p0} all starts from one on the right of the curves, as they are all normalized with respect to their own nozzle total pressure $P_{j,0}$.

The c_{p0} values from different flight conditions fall to roughly 0.015 at around $s = -0.024$ m. The number 0.015 comes from $PRs = 60$ as $P_{s,0}/P_{j,0} = 1/(PRs) = 1/60 \approx 0.017$. This sharp decline of the total pressure implies the formation of a strong compression wave, which is observable in Figure 13(a), namely, the outer bow shock for the free flow and the Mach disk for the jet flow. Due to the energy
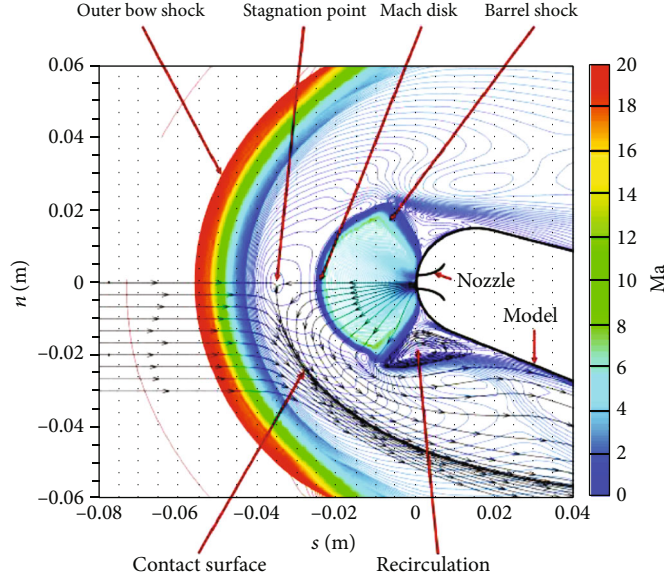
FIGURE 10: Mach number contour lines with streamlines for cases H70Ma20-J.

TABLE 4: Summary of computed surface heat transfer properties (with ^ meaning the same as above).

No.	Label	Suffix	St	$\dot{Q}_{max}$ (kW/m^2)	$\dot{Q}N_{max}$	$x_{\dot{Q}N\ max}/l$	$x_{\dot{Q}N=0.1}/l$
1	H70Ma20	NJ	0.478752	3,691.960	1	0.3%	
2	^	AoA0	0.043343	334.242	0.090532	100.0%	100.0%
3	^	AoA10	0.049797	384.018	0.104015	100.0%	99.8%
4	^	J/AoA20	0.124530	960.326	0.260113	94.1%	58.2%
5	^	AoA30	0.145992	1,125.830	0.304942	53.1%	29.3%
6	^	AoA40	0.187119	1,443.000	0.390848	27.6%	12.8%
7	H60Ma15	NJ	0.247624	3,598.680	1	0.3%	
8	^	J	0.074647	1,084.840	0.301454	88.3%	57.1%
9	H50Ma10	NJ	0.142243	2,333.530	1	0.3%	
10	^	Jet5	0.038680	634.550	0.271927	27.3%	11.9%
11	^	Jet15	0.039563	649.034	0.278134	41.4%	23.5%
12	^	Jet30	0.041883	687.093	0.294444	59.0%	34.7%
13	^	Jet45	0.043795	718.467	0.307889	70.7%	41.3%
14	^	J/Jet60	0.044842	735.651	0.315253	82.4%	51.1%
15	H40Ma5	NJ	0.071686	490.049	1	0.3%	
16	^	AoA0	0.010700	73.147	0.149265	100.0%	58.6%
17	^	AoA10	0.012582	86.013	0.175519	100.0%	47.2%
18	^	J/AoA20	0.017601	120.320	0.245527	82.4%	35.6%
19	^	AoA30	0.023159	158.314	0.323058	47.3%	18.5%
20	^	AoA40	0.034015	232.528	0.474499	24.1%	6.6%

dissipating nonisentropic compression, the jet reaches agreement with the free flow behind the bow shock in terms of total pressure.

Taking the first derivative of c_{p0} along the center line ($n = 0$) in the jet direction (s direction) to assess the actual location of the shock, two groups of peak are visible in the plot of $d(c_{p0})/ds$ in Figure 14(a). The larger one on the left indicates the free flow bow shock location, and the small one on the right represents the jet flow Mach disk. Figure 14(b) provides a zoomed-in view of the smaller group of peak. The convergence of the $d(c_{p0})/ds$ peaks (i.e., the Mach disk locations) from different altitudes at $s \approx -0.0235$ m is clear.

As expected from the theoretical analysis in Section 2.1, plots of the c_{p0} and $d(c_{p0})/ds$ again confirmed the advantages of employing the PRs as the jet design parameter. With the
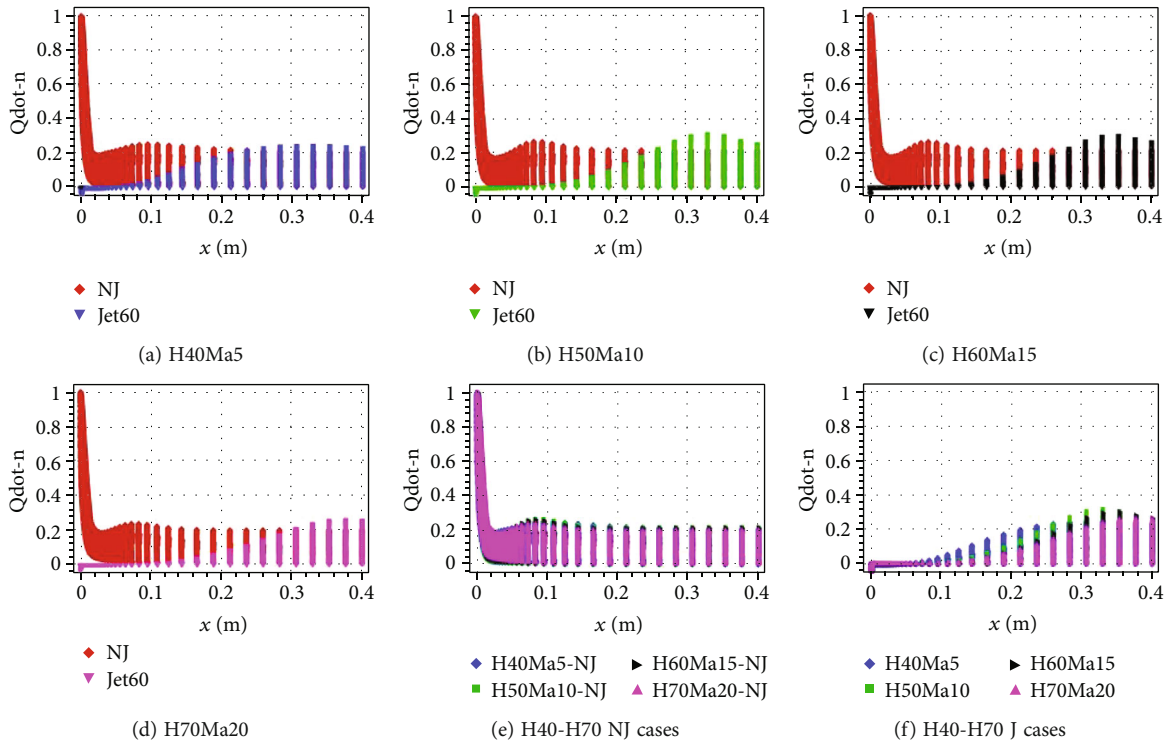
(a) H40Ma5

(b) H50Ma10

(c) H60Ma15

(d) H70Ma20

(e) H40-H70 NJ cases

(f) H40-H70 J cases

Figure 11: Comparison of the $\dot{Q}N$ values from the NJ and J cases under different flight conditions and different heights.
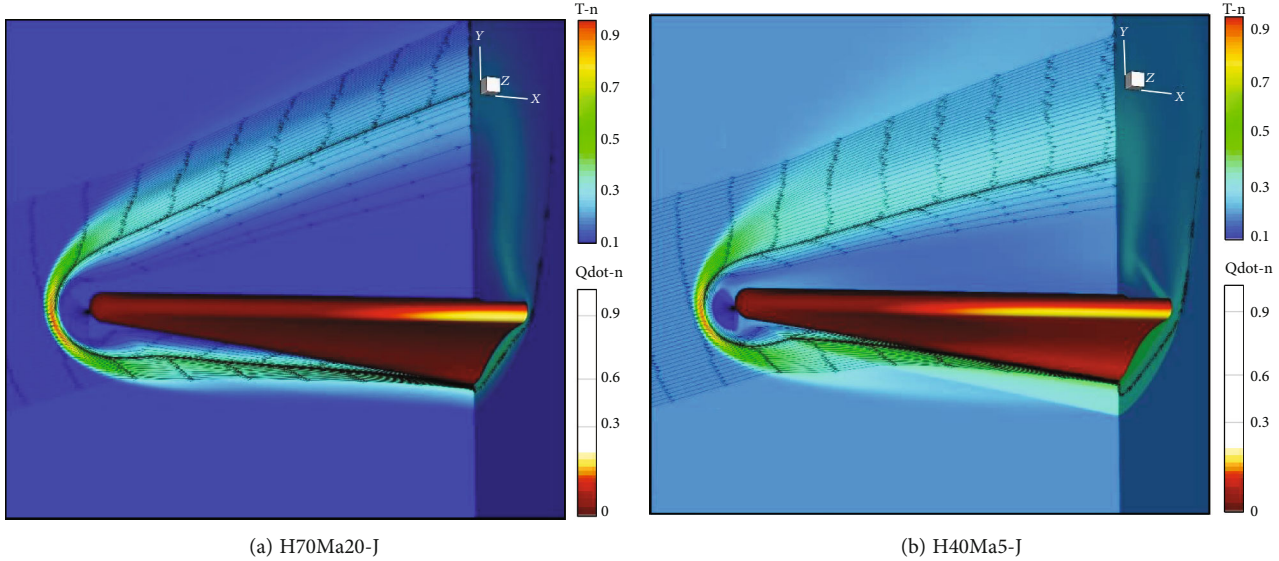

(a) H70Ma20-J

(b) H40Ma5-J

Figure 12: Normalized flow field temperature contour and streamlines and model surface heat flux contour of two different flight conditions.

help of a constant *PRs*, the same Mach disk location under any different flight conditions could be guaranteed. This property could help the *PRs*AJ-TPS maintain a rather stable protection effect in various flight situations. Evaluation of the jet mass flow rate $\dot{m}$ and total coolant consumption could also be addressed immediately after the HFV trajectory is determined.

4.3. *Influence of Different PRs Values.* In this section, the influence of different *PRs* on the thermal protection intensity and efficiency is analyzed based on case 9–14 (the H50Ma10 series). Table 4 has already revealed that the protection range increases with the *PRs* ratio, yet the resulting peak heat flux also increases slightly.
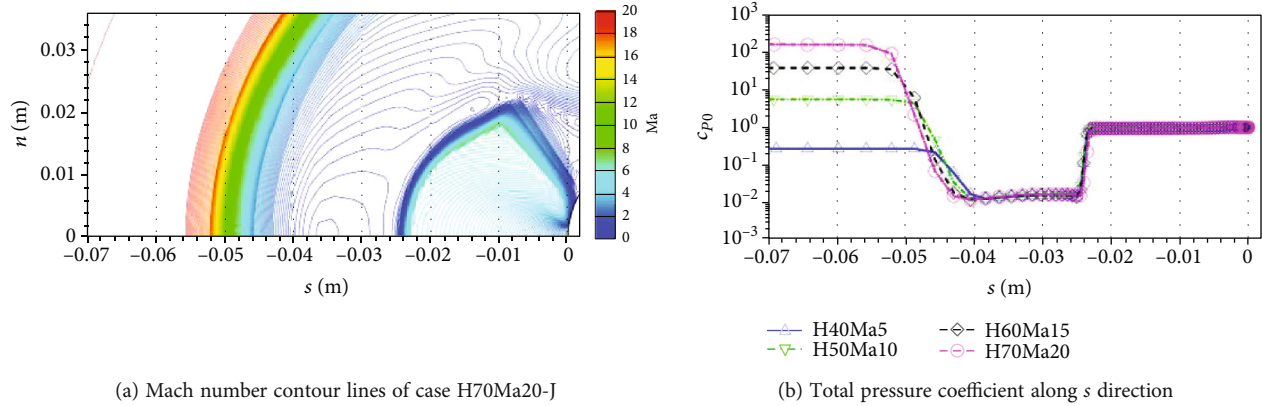
(a) Mach number contour lines of case H70Ma20-J

(b) Total pressure coefficient along s direction

FIGURE 13: Typical jet flow structure and total pressure coefficient analysis along s direction.

(a) Overview

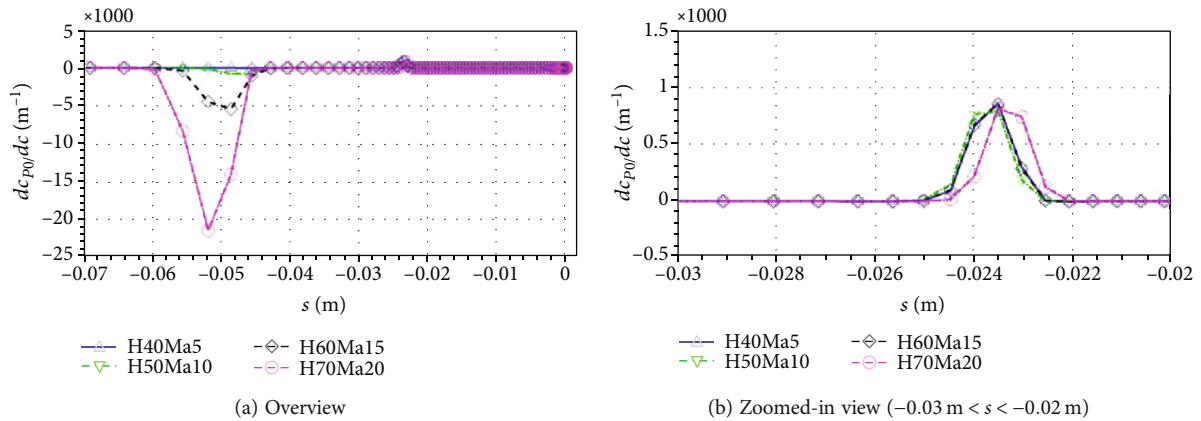(b) Zoomed-in view ($-0.03\,\mathrm{m} < s < -0.02\,\mathrm{m}$)

FIGURE 14: Analysis of the 1st order derivatives of the total pressure coefficients along s direction.

Figure 15 depicts the flow field of different *PRs*. The first impression is clear that the jet flow dominated area ahead of the nose tip expands with the growth of the *PRs*, and the external bow shock is expelled further off the stagnation point.

With *PRs* = 5, the jet protects only a small part of the model. The heat flux distribution on the rest of the model surface remains generally unchanged compared with the "NJ" case. The jet flow expansion fan is rather small in the Jet5 case. As the *PRs* starts to increase, the cooled area created by the jet flow steadily spreads and drives the region of high heat flux on the leading-edge continuously backward. The turning shock formed together by the reversed jet flow, and the free flow also becomes hazier and weaker, since more coolant is injected into the flow field and the cool jet flow layer becomes thicker.

Analyzing the surface heat flux distribution in *x*-direction (Figure 16), such trend is even more apparent. With the active jet in operation, the significantly high heat flux at the stagnation point is completely erased. The new peak heat flux on the leading edge also grows as the *PRs* increases, but to a trivial extent. Such a deterioration of thermal protection intensity is not welcomed and is most probably brought about by the geometric shape of this specific model.

The convex-concave shape transition of the fuselage-wing blending surface grows more concave near the bottom, and the leading edge is seemingly more protruding. The growing amount of jet flow forms a larger cooling bubble and disturbs more free flow. The resulting stronger shear layer flushes the more protruding grown leading edge harder at downstream, causing a noticeable hot spot of aerodynamic heating.

Since the *PRs* ratio determines the jet total pressure based on the free flow condition, the mass flow rate of the sonic nozzle applied in the current design could be obtained. Table 5 gives the mass flow rate $\dot{m}$ of each case in the H50Ma10 series.

Figure 17 plots the change of $\dot{Q}N_{\mathrm{max}}$, $x_{\dot{Q}N_{\mathrm{max}}}/l$, and $x_{\dot{Q}N=0.1}/l$ with respect to $\dot{m}$. Apparently, the peak heat flux without the *PRs*AJ-TPS is quite large. When the *PRs*AJ-TPS is active, the peak heat flux drops considerably. Starting from $\dot{m} \approx 1.51\mathrm{E} - 03\,\mathrm{kg/s}$ (the Jet5 case), all three indicators grow almost linearly with the minimum regression coefficient R^2 being 0.976. This implies that at least from the Jet5 case, the efficiency of *PRs*AJ-TPS is the same for every $\dot{m}$.

What else needs to be noticed is that there might exist a minimum value of *PRs* below *PRs* = 5, which could just be enough to purge the peak heat flux of the "NJ" case at the

(a) NJ case

(b) Jet5 case (PRs = 5)

(c) Jet15 case (PRs = 15)

(d) Jet30 case (PRs = 30)

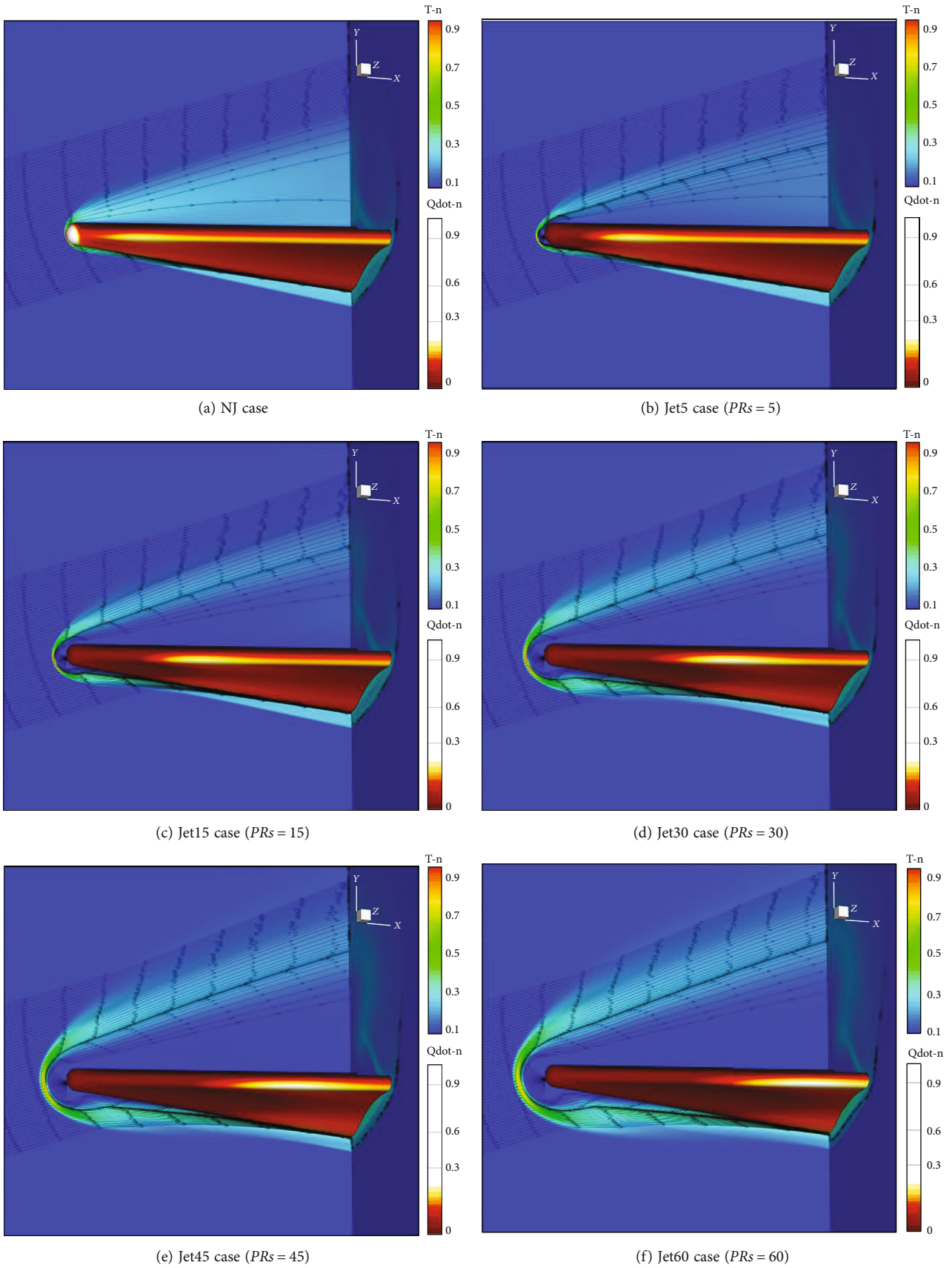(e) Jet45 case (PRs = 45)

(f) Jet60 case (PRs = 60)

FIGURE 15: Normalized flow field temperature contour and streamlines and model surface heat flux contour of the H50Ma10 series.
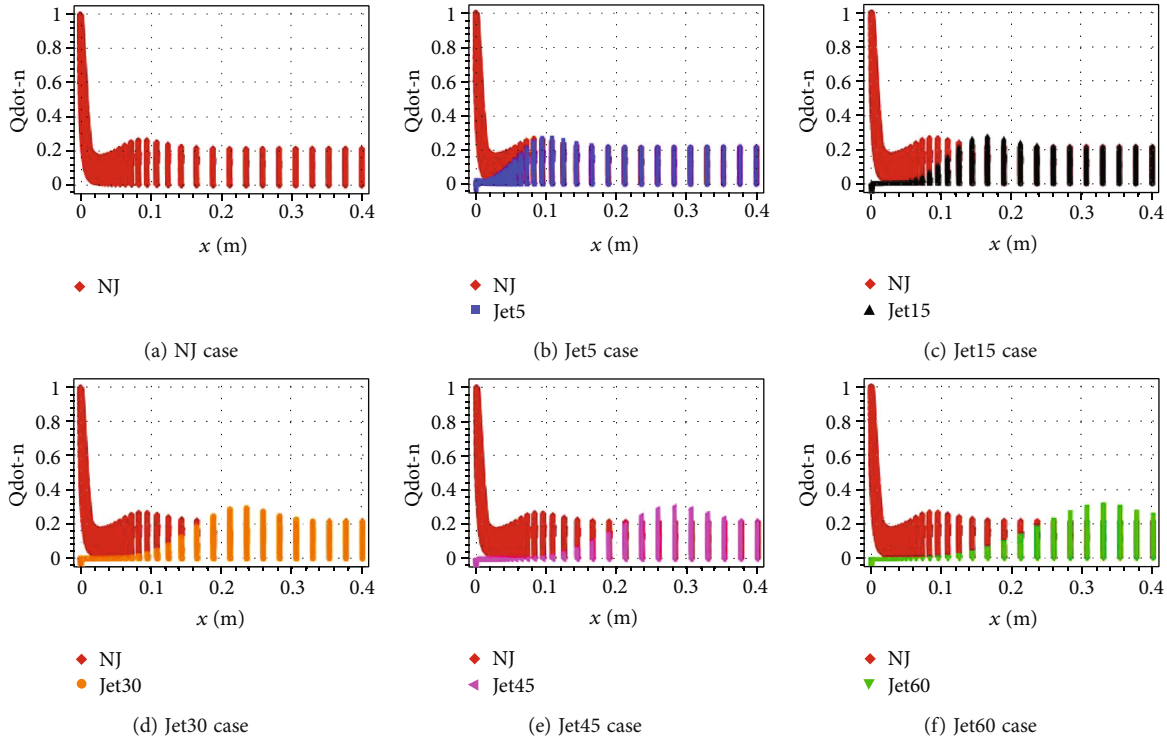
Figure 16: $\dot{Q}N$ value of the NJ and J cases for different *PRs* of the H50Ma10 series.

Table 5: Mass flow rates of the H50Ma10 series.

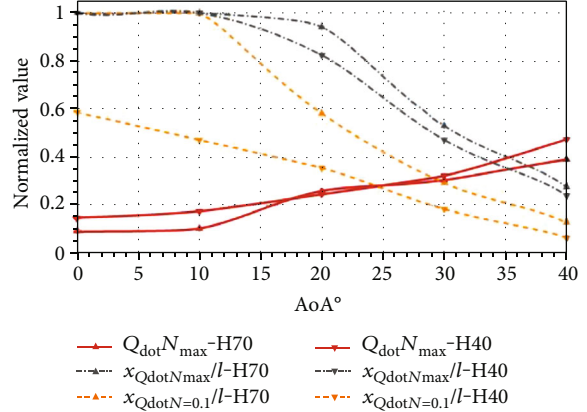| No.	Label	Suffix	$\dot{m}$ (kg/s)
10	H50Ma10	Jet5	1.51E − 03
11	∧	Jet15	4.53E − 03
12	∧	Jet30	9.07E − 03
13	∧	Jet45	1.36E − 02
14	∧	J/Jet60	1.81E − 02

Figure 18: Plots of key indicators against angle of attack for the H70Ma20 and H40Ma5 series.

stagnation point. When the *PRs* continues to drop, the *PRs*AJ-TPS may finally behave as a single jet film or a transpiration cooling strategy. The jet exerts almost no visible influence on the free flow field structure and simply spreads radially to cover the model head as [10] expected. However, the *PRs*AJ-TPS studied here could provide extensive and high-level thermal protection. It is also more robust against attitude variation as will be illustrated in the next subsection.

4.4. Influence of Different Angles of Attack. As the current design of *PRs*AJ-TPS employs only a single nozzle, concerns regarding the stability of the protection intensity and range
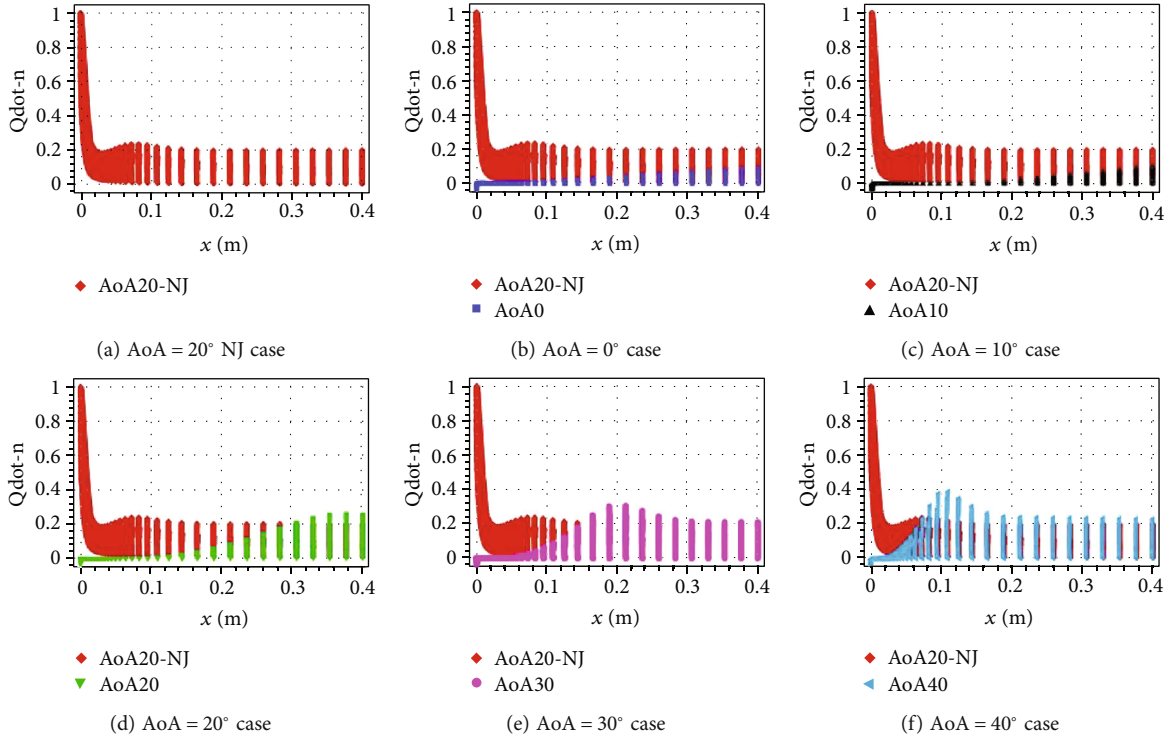

Figure 17: Plot of key indicators against $\dot{m}$ for the H50Ma10 series.

(a) AoA = 20° NJ case

(b) AoA = 0° case

(c) AoA = 10° case

(d) AoA = 20° case

(e) AoA = 30° case

(f) AoA = 40° case

FIGURE 19: $\dot{Q}N$ values of the NJ and J cases for different AoAs of the H70Ma20 series.

(a) AoA = 20° NJ case

(b) AoA = 0° case

(c) AoA = 10° case

(d) AoA = 20° case
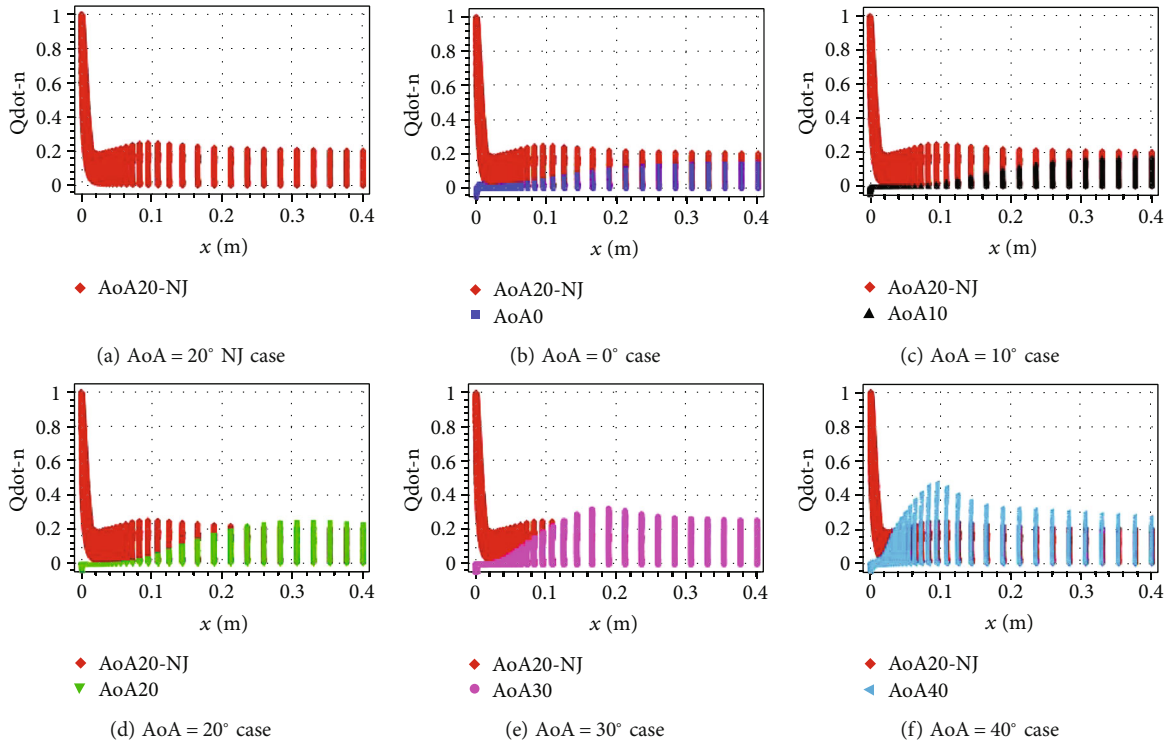
(e) AoA = 30° case

(f) AoA = 40° case

FIGURE 20: $\dot{Q}N$ values of the NJ and J cases for different AoAs of the H40Ma5 series.

under various HFV attitudes raise naturally. To address such concerns, the jet nozzle is designed to be tilted and a large *PRs* is chosen. The influence of different angles of attack

on the *PRs*AJ-TPS performance is analyzed based on the results of case 1–6 (the H70Ma20 series) and case 15–20 (the H40Ma5 series). Table 4 gives some key figures

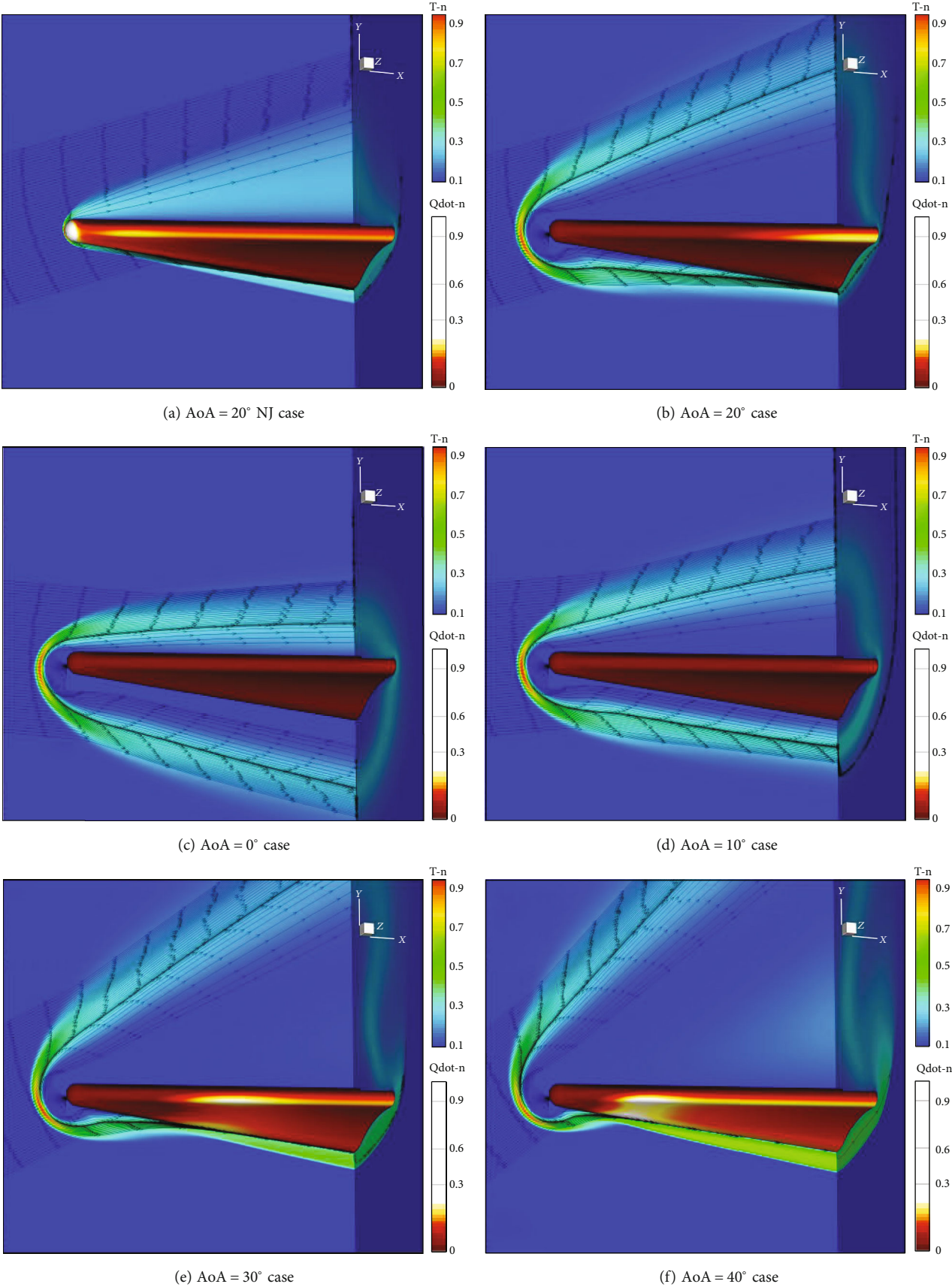(a) AoA = 20° NJ case

(b) AoA = 20° case

(c) AoA = 0° case

(d) AoA = 10° case

(e) AoA = 30° case

(f) AoA = 40° case

Figure 21: Normalized flow field temperature contour and streamlines and model surface heat flux contour of the H70Ma20 series.

(a) AoA = 20° NJ case

(b) AoA = 20° case

(c) AoA = 0° case

(d) AoA = 10° case

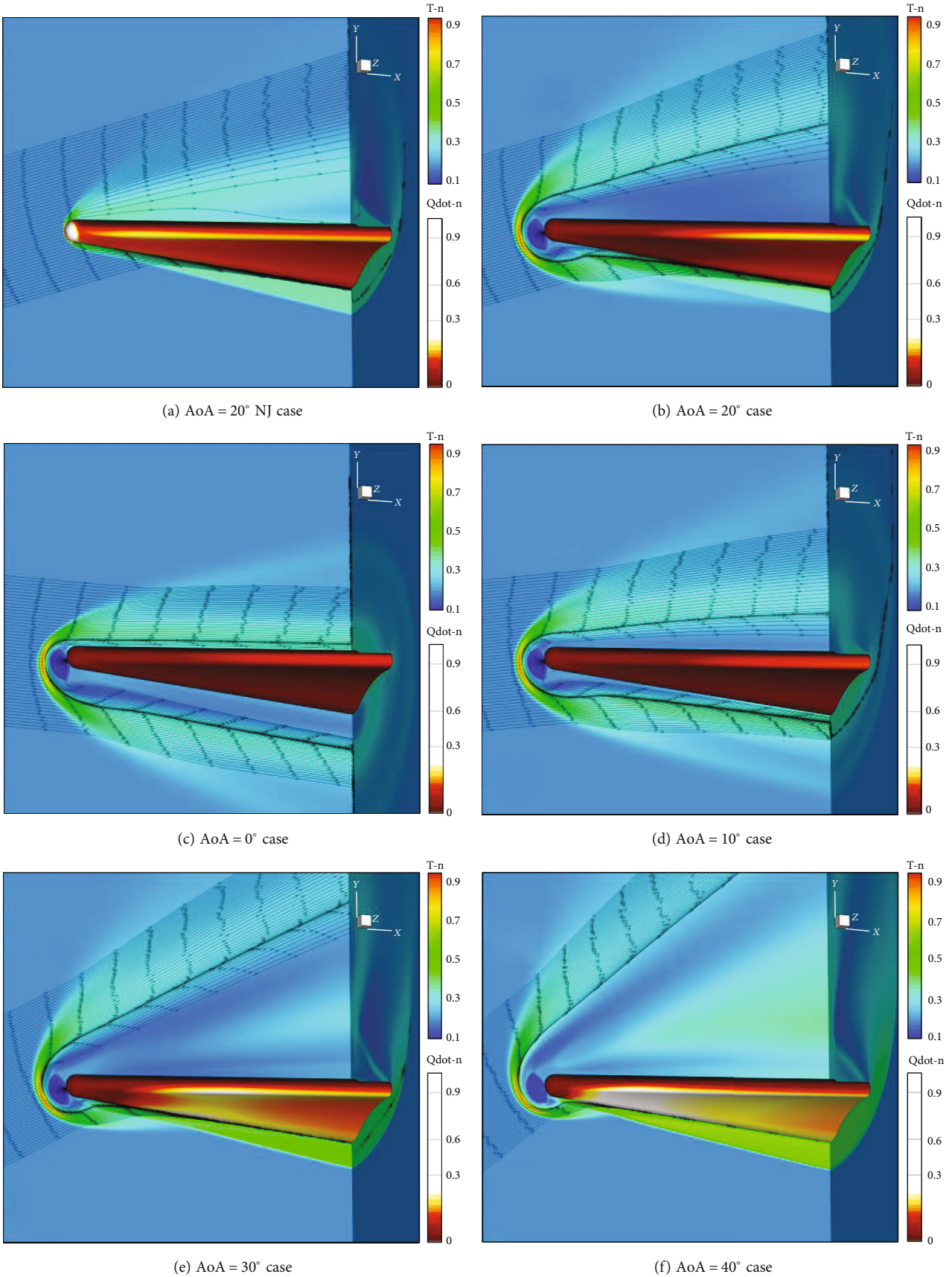(e) AoA = 30° case

(f) AoA = 40° case

Figure 22: Normalized flow field temperature contour and streamlines and model surface heat flux contour of the H40Ma5 series.

regarding the thermal protection capability of these two case series. Figure 18 plots the performance indicators with respect to the angle of attack.

The calculation results for both series follow a similar pattern with respect to the angle of attack. Yet, the thermal protection effect is weaker in the H40Ma5 series, since the $\dot{Q}N_{\max}$ (solid lines) in this series generally exceeds that in the H70Ma20 series. The reason might be that the Reynolds number is much larger at the lower flight altitude. Therefore, the inertial force dominated the area away from the main interaction region at H40Ma5 condition, resulting in higher $\dot{Q}N_{\max}$ and clear formation of the reattachment shock, while at H70Ma20 conditions, viscosity plays a major role. The reattachment wave is thus blurred, and the relative heating ($\dot{Q}N_{\max}$) is less serious. This also explains why that the protection range indicators from H40Ma5 generally sit below the ones from H70Ma20.

Turning toward the direction of a decreasing AoA from 20°, the results are remarkable. In the H70Ma20 series, $\dot{Q}N_{\max}$ the peak heat flux values on the nose model from both the AoA0 and AoA10 cases are reduced to around 10% of the "NJ" case with their locations ($x_{\dot{Q}N_{\max}}/l$) resting at the end of the model. Similar results can also be found in the corresponding cases in the H40Ma5 series, but with higher $\dot{Q}N_{\max}$ values.

The more stringent indicator $x_{\dot{Q}N=0.1}/l$ (dashed lines) grows with a decreasing AoA in both case series. However, it only reaches 58.6% of the body length in the H40Ma5 series, while in the H70Ma20 series, $x_{\dot{Q}N=0.1}/l$ also equals 1. This implies the *PRs*AJ-TPS may have reached a thermal protection capability ceiling at a low aerodynamic heating condition, no further reduction of heat flux is possible as the "NJ" case peak heat flux is already quite low.

When the AoA increases from 20° to 40°, the peak heat flux increases. The $\dot{Q}N_{\max}$ for the AoA40 case has increased by 50% with respect to that in the AoA20 case in the H70Ma20 series and almost doubled in the H40Ma5 Series. The protection range indicators $x_{\dot{Q}N_{\max}}/l$ and $x_{\dot{Q}N=0.1}/l$ also shrink significantly to 27.6% and 12.8% at AoA40 in the H70Ma20 series, to 24.1% and 6.6% in the H40Ma5 series. Figures 19 and 20 plot the $\dot{Q}N$ values of the "NJ" and "J" cases. The values are taken from every mesh point on the nose model and are plotted along the x-direction. The overall distribution of surface heat flux on the model body is similar for both series. It is also apparent that at low angles of attack, the *PRs*AJ-TPS offers extraordinarily good thermal protection, and the positive effect remains acceptable until AoA = 30°.

From Figures 21 and 22 below, the jet from the *PRs*AJ-TPS creates a cooled region embracing the model, as if there is a virtual blunt body shielding the nose model. The part of the nose model that falls within the virtual blunt body is then protected by the surrounding cool jet flow. Otherwise, a heated region is established at the place of intersection between the model and the virtual blunt body, which is also the place of flow reattachment. The turning shock resulting from flow reattachment is especially evident in the AoA30 and AoA40 cases from both series.

The turning shock-induced high heat flux first appears on the leading edge, then the lower surface center line, and finally on the transition surface between them. On the other hand, the lee side of the model is always cool under a positive angle of attack.

From the streamline figure of case AoA = 0° in the H70Ma20 series, the reason why the *PRs*AJ-TPS performs so much better under smaller angles of attack is conspicuous. As the jet direction deviates from the free flow direction for 20° downward, the majority of the jet flow is confined to the lower surface of the HFV compared with larger AoA scenarios. With more coolant being gathered to the more severely aerodynamic heated windward side of the HFV, a more intense cooling effect is naturally achieved. Furthermore, with a decreased angle of attack, the nose tip undertakes a larger part of the aerodynamic heating. Consequently, the rest of the body is cooler. After the *PRs*AJ-TPS starts working, the peak heat flux on the nose tip is also removed, and the aerodynamic heating problem is partially relieved. Adding all these factors together, the overall thermal protection effect then looks rather astonishing when the angle of attack declines.

Oppositely, with an increasing angle of attack from the nominal value, less coolant spreads to the severely heated windward side of the HFV. Most of the jet is flushed upward to the cool leeward surface and is wasted, leading to a diminished overall thermal protection effect. The location of the peak heat flux also moves forward rather than backwards. Its intensity increases with an increasing AoA, since the free flow impinges on the model surface with a larger incidence angle. The performance of the *PRs*AJ-TPS is thus degraded with a positive offset from the nominal angle of attack.

The above information provides valuable information on the design and application of the jet based active TPS. Suppose an HFV flies at an angle of attack ranging from α_1 to α_2, with $0° < \alpha_2 - \alpha_1 < 20°$; then, the HFV designer should align the nozzle in the direction parallel to α_2 for better *PRs*AJ-TPS performance.

5. Conclusions

In this study, a new jet design parameter *PRs*-based active jet thermal protection system, the *PRs*AJ-TPS, is designed and its performance is numerically investigated. The *PRs*AJ-TPS employs a new jet total pressure ratio *PRs* and a tilted arrangement of the jet nozzle. The advantages of the new parameter *PRs* have been theoretically analyzed and numerically verified under different flight conditions along an HFV trajectory. The influences of different *PRs* values (maintained the short penetration mode of the opposing jet throughout the study) and angles of attack on the *PRs*AJ-TPS performance have also been investigated. The following conclusions are reached:

(1) Theoretical analysis and numerical results have proved that by employing the *PRs* as the jet design parameter, and an identical jet flow Mach disk location could be obtained for quite different free flow conditions with the same *PRs*, which provides a single and simple guidance on the active jet design for HFVs

(2) The *PRs*AJ-TPS is capable of removing the severe aerodynamic heating on the nose model effectively and extensively, as an average peak heat flux reduction of 72% and a rearward shift of the $\dot{Q}_{\mathrm{max}}$ by at least 82% of the model length are achieved for the "J" cases

(3) A constant total pressure ratio *PRs* will result in a specific jet flow Mach disk location even under vastly different flight conditions

(4) When the *PRs*AJ-TPS is in operation, the maximum surface heat flux $\dot{Q}_{\mathrm{max}}$ increases slightly with an increasing *PRs*, while the thermal protection range indicators $x_{\dot{Q}N_{\mathrm{max}}}/l$ and $x_{\dot{Q}N=0.1}/l$ increase almost linearly

(5) The tilted and with the nominal flight angle of attack aligned arrangement of the *PRs*AJ-TPS nozzle could provide robust thermal protection against the variation of angle of attack, especially when the angle of attack decreases, since the peak heat flux reduction could drop over 90% and the peak heat flux locates at the model bottom

The focus of further research will be the selection of an optimum coolant and the *PRs*AJ-TPS integrated leading-edge protection strategy. There is also a wind tunnel test in progress for the validation of the *PRs*AJ-TPS concept.

Data Availability

The data used to support the findings of this study are included within the article.

Conflicts of Interest

The authors declare that there is no conflicts of interest regarding the publication of this paper.

Acknowledgments

References

[1] D. A. Stewart and D. B. Leiser, "Toughened uni-piece, fibrous, reinforced, oxidization-resistant composite," in *The United States of America as Represented by the Administrator of the National Aeronautics and Space Administration (NASA)*, Washington, DC, USA, 2008.

[2] W. Huang, R.-R. Zhang, L. Yan, M. Ou, and R. Moradi, "Numerical experiment on the flow field properties of a blunted body with a counterflowing jet in supersonic flows," *Acta Astronautica*, vol. 147, pp. 231–240, 2018.

[3] D. Knight, J. Longo, D. Drikakis et al., "Assessment of CFD capability for prediction of hypersonic shock interactions," *Progress in Aerospace Sciences*, vol. 48-49, pp. 8–26, 2012.

[4] W. Xie, Z. Luo, Y. Zhou, W. Peng, Q. Liu, and D. Wang, "Experimental and numerical investigation on opposing plasma synthetic jet for drag reduction," *Chinese Journal of Aeronautics*, vol. 35, no. 8, pp. 75–91, 2022.

[5] W. Xie, Z. Luo, L. Hou, Y. Zhou, Q. Liu, and W. Peng, "Characterization of plasma synthetic jet actuator with Laval-shaped exit and application to drag reduction in supersonic flow," *Physics of Fluids*, vol. 33, no. 9, article 096104, 2021.

[6] H. Böhrk, H. Elsässer, and H. Weihs, "The SHEFEX II thermal protection system," in *7th European Symposium on Aerothermodynamics*, p. 96, Brugge, Belgium, 2011.

[7] H. Böhrk, C. Dittert, H. Weihs, T. Thiele, and A. Guelhan, "Thermal testing of the sharp leading edge of SHEFEX II," in *18th AIAA/3AF International Space Planes and Hypersonic Systems and Technologies Conference*, p. 5919, Tours, France, 2012.

[8] H. Böhrk, "Transpiration cooling at hypersonic flight - AKTiV on SHEFEX II," in *11th AIAA/ASME Joint Thermophysics and Heat Transfer Conference*, p. 2676, Atlanta, GA, USA, 2014.

[9] H. M. McMahon, *An Experimental Study of the Effect of Mass Injection at the Stagnation Point of a Blunt Body*, Guggenheim Aeronautical Laboratory, California Institute of Technology, 1958.

[10] E. B. Klunker and H. R. Ivey, *An Analysis of Supersonic Aerodynamic Heating with Continuous Fluid Injection*, National Aeronautics and Space Administration Hampton VA Langley Research Center, 1949.

[11] C. H. E. Warren, *An Experimental Investigation of the Effect of Ejecting a Coolant Gas at the Nose of a Blunt Body*, Guggenheim Aeronautical Laboratory, California Insitute of Technology, Pasadena, CA, USA, 1958.

[12] P. J. Finley, "The flow of a jet from a body opposing a supersonic free stream," *Journal of Fluid Mechanics*, vol. 26, no. 2, pp. 337–368, 1966.

[13] K. Hayashi and S. Aso, "Effect of pressure ratio on aerodynamic heating reduction due to opposing jet," in *33rd AIAA Fluid Dynamics Conference and Exhibit*, p. 4041, Orlando, Florida, USA, 2003.

[14] E. O. Daso, V. E. Pritchett, T.-S. Wang, D. K. Ota, I. M. Blankson, and A. H. Auslender, "Dynamics of shock dispersion and interactions in supersonic freestreams with counterflowing jets," *AIAA Journal*, vol. 47, no. 6, pp. 1313–1326, 2009.

[15] D.-M. Kim, Y. Kim, T.-S. Roh, and H. J. Lee, "Observation of unsteady motion induced by counterflow jet on blunt body in hypersonic flow," *Journal of Visualization*, vol. 25, no. 1, pp. 1–14, 2022.

[16] V. Kulkarni and K. P. J. Reddy, "Effect of a supersonic counterflow jet on blunt body heat transfer rates for oncoming high enthalpy flow," *Journal of Engineering Physics and Thermophysics*, vol. 82, no. 1, pp. 1–5, 2009.

[17] T. Imoto, H. Okabe, and Y. Tani, "Enhancement of aerodynamic heating reduction in high enthalpy flows with opposing jet," in *49th AIAA Aerospace Sciences Meeting including the New Horizons Forum and Aerospace Exposition*, p. 346, Orlando, Florida, USA, 2011.

[18] N. Morimoto, S. Aso, and Y. Tani, "Reduction of aerodynamic heating and drag with opposing jet through extended nozzle in high enthalpy flow," in *Proceedings of the 29th Congress of the International Council of the Aeronautical Sciences*, pp. 1–9, Petersburg, Russia, 2014.

[19] Z. Ce, R. Tomita, K. Suzuki, and Y. Watanabe, "Effect of opposing multiphase jet on hypersonic flow around blunt body," *IOP Conference Series: Materials Science and Engineering*, vol. 249, article 012014, 2017.

[20] Y. Rong, J. Sun, W. Liu, and R. Zhan, "Heat flux reduction research in hypersonic flow with opposing jet," *International Journal of Aerospace and Mechanical Engineering*, vol. 6, no. 8, pp. 1786–1790, 2012.

[21] S. Li, Z. Wang, W. Huang, and J. Liu, "Drag and heat reduction performance for an equal polygon opposing jet," *Journal of Aerospace Engineering*, vol. 30, no. 1, 2017.

[22] S. Li, Z. Wang, W. Huang, and J. Liu, "Effect of the injector configuration for opposing jet on the drag and heat reduction," *Aerospace Science and Technology*, vol. 51, pp. 78–86, 2016.

[23] S. Li, Z. Wang, W. Huang, and L. Yan, "Analysis of flowfield characteristics for equal polygon opposing jet on different freeflow conditions," *Acta Astronautica*, vol. 133, pp. 50–62, 2017.

[24] S. Li, Z. Wang, G. N. Barakos, W. Huang, and R. Steijl, "Research on the drag reduction performance induced by the counterflowing jet for waverider with variable blunt radii," *Acta Astronautica*, vol. 127, pp. 120–130, 2016.

[25] X. Sheng, X. Lu, and J. Zhang, "Numerical study on combined thermal protection system on hypersonic vehicle and structure parameters influence of acoustic cavity," in *2021 12th International Conference on Mechanical and Aerospace Engineering (ICMAE)*, pp. 343–347, Athens, Greece, 2021.

[26] J. Huang and B. Fan, "Coupled fluid–thermal investigation on active thermal protection system by opposing jet," *Journal of Spacecraft and Rockets*, vol. 59, no. 3, pp. 1033–1038, 2022.

[27] S. B. H. Shah and X.-Y. Lu, "Computational study of drag reduction at various freestream flows using a counterflow jet from a hemispherical cylinder," *Engineering Applications of Computational Fluid Mechanics*, vol. 4, no. 1, pp. 150–163, 2010.

[28] C. Zhou and W. Ji, "A three-dimensional numerical investigation on drag reduction of a supersonic spherical body with an opposing jet," *Proceedings of the Institution of Mechanical Engineers, Part G: Journal of Aerospace Engineering*, vol. 228, no. 2, pp. 163–177, 2014.

[29] S. S. Kanwar, G. Dubey, M. Singh, and G. S. Khanday, "Numerical investigation of drag reduction by opposite supersonic jet for a large angle blunt cone at Mach 8.0," *International Journal of Research in Engineering and Applied Sciences*, vol. 5, no. 6, pp. 223–233, 2015.

[30] P. Harmon, A. Vashishtha, D. Callaghan, C. Nolan, and R. Deiterding, "Study of direct gas injection into stagnation zone of blunt nose at hypersonic flow," in *AIAA Propulsion and Energy 2021 Forum, American Institute of Aeronautics and Astronautics*, p. 3529, Virtual Event, 2021.

[31] J. Guo, G. Lin, X. Bu, and H. Li, "Sensitivity analysis of flowfield modeling parameters upon the flow structure and aerodynamics of an opposing jet over a hypersonic blunt body," *Chinese Journal of Aeronautics*, vol. 33, no. 1, pp. 161–175, 2020.

[32] C. Ji, B. Liu, W. Huang, S. Li, and L. Yan, "Investigation on the drag reduction and thermal protection properties of the porous opposing jet in the supersonic flow: a parametric study with constant mass flow rate," *Aerospace Science and Technology*, vol. 118, article 107064, 2021.

[33] C. Ji, B. Liu, S. Li, W. Huang, and L. Yan, "Parametric investigation on drag reduction and thermal protection characteris-tics of the porous opposing jet in the hypersonic flow," *Aerospace Science and Technology*, vol. 116, article 106867, 2021.

[34] Z. Wang and X. Zhang, "Parametric research on drag reduction and thermal protection of blunt-body with opposing jets of forward convergent nozzle in supersonic flows," *Acta Astronautica*, vol. 190, pp. 218–230, 2022.

[35] M. Barzegar Gerdroodbary, "Numerical analysis on cooling performance of counterflowing jet over aerodisked blunt body," *Shock Waves*, vol. 24, no. 5, pp. 537–543, 2014.

[36] M. Barzegar Gerdroodbary and S. M. Hosseinalipour, "Numerical simulation of hypersonic flow over highly blunted cones with spike," *Acta Astronautica*, vol. 67, no. 1-2, pp. 180–193, 2010.

[37] B. Shen and W. Liu, "Thermal protection performance of opposing jet generating with solid fuel," *Acta Astronautica*, vol. 144, pp. 90–96, 2018.

[38] B. Shen and W. Liu, "Effect of hot fuel gas on a combinational opposing jet and platelet transpiration thermal protection system," *Applied Thermal Engineering*, vol. 164, article 114513, 2020.

[39] B. Shen, L. Yin, H. Liu, and W. Liu, "Thermal protection characteristics for a combinational opposing jet and platelet transpiration cooling nose-tip," *Acta Astronautica*, vol. 155, pp. 143–152, 2019.

[40] W. Zhang, X. Wang, Z. Zhang, and T. Su, "Transient numerical simulation of hemispherical cone with combined opposing jet in hypersonic flow," *Acta Astronautica*, vol. 175, pp. 327–337, 2020.

[41] W. Zhang, X. Wang, Z. Zhang, F. Han, and S. Zhao, "Heat and drag reduction of single and combined opposing jets in hypersonic nonequilibrium flows," *Aerospace Science and Technology*, vol. 121, article 107194, 2022.

[42] Y. Liu and Z. Jiang, "Concept of non-ablative thermal protection system for hypersonic vehicles," *AIAA Journal*, vol. 51, no. 3, pp. 584–590, 2013.

[43] J. Huang and W.-X. Yao, "Active flow control by a novel combinational active thermal protection for hypersonic vehicles," *Acta Astronautica*, vol. 170, pp. 320–330, 2020.

[44] M. Ou, L. Yan, W. Huang, S. B. Li, and L. Q. Li, "Detailed parametric investigations on drag and heat flux reduction induced by a combinational spike and opposing jet concept in hypersonic flows," *International Journal of Heat and Mass Transfer*, vol. 126, pp. 10–31, 2018.

[45] R. Moradi, M. Mosavat, M. Barzegar Gerdroodbary, A. Abdollahi, and Y. Amini, "The influence of coolant jet direction on heat reduction on the nose cone with Aerodome at supersonic flow," *Acta Astronautica*, vol. 151, pp. 487–493, 2018.

[46] F. Pish, R. Moradi, A. Edalatpour, and M. Barzegar Gerdroodbary, "The effect of coolant injection from the tip of spike on aerodynamic heating of nose cone at supersonic flow," *Acta Astronautica*, vol. 154, pp. 52–60, 2019.

[47] W. Fan, S. Li, J. Zhou, W. Huang, M. Ou, and R. Zhang, "Study on the drag and heat reduction performance of porous opposing jet in hypersonic flow," *International Journal of Heat and Mass Transfer*, vol. 139, pp. 351–361, 2019.

[48] X. Sun, Z. Guo, W. Huang, S. Li, and L. Yan, "Drag and heat reduction mechanism induced by a combinational novel cavity and counterflowing jet concept in hypersonic flows," *Acta Astronautica*, vol. 126, pp. 109–119, 2016.

[49] X. Sun, Z. Guo, W. Huang, S. Li, and L. Yan, "A study of performance parameters on drag and heat flux reduction efficiency of combinational novel cavity and opposing jet concept in hypersonic flows," *Acta Astronautica*, vol. 131, pp. 204–225, 2017.

[50] X. Sun, W. Huang, M. Ou, R. Zhang, and S. Li, "A survey on numerical simulations of drag and heat reduction mechanism in supersonic/hypersonic flows," *Chinese Journal of Aeronautics*, vol. 32, no. 4, pp. 771–784, 2019.

[51] Y. Meng, L. Yan, W. Huang, and Z. Wang, "Fluid-thermal coupled investigation on the combinational spike and opposing/lateral jet in hypersonic flows," *Acta Astronautica*, vol. 185, pp. 264–282, 2021.

[52] Y. Meng, L. Yan, W. Huang, and Z. Zhao, "Coupled investigation on drag and heat flux reduction over spiked waverider with a wide-speed range," *Acta Astronautica*, vol. 182, pp. 498–516, 2021.

[53] L. Zhu, X. Tian, W. Li, M. Yan, X. Tang, and M. Huang, "Non-ablative dual-jet strategy for drag and heat reduction of hypersonic blunt vehicles," *Journal of Aerospace Engineering*, vol. 34, no. 5, p. 04021052, 2021.

[54] K. Hayashi, S. Aso, and Y. Tani, "Numerical study of thermal protection system by opposing jet," in *43rd AIAA Aerospace Sciences Meeting and Exhibit*, p. 188, Reno, Nevada, USA, 2005.

[55] F. R. Menter, "Zonal two equation kw turbulence models for aerodynamic flows," in *24th Fluid Dynamics Conference*, p. 2906, Orlando, Florida, USA, 1993.

[56] K. He, J. Chen, and W. Dong, "Penetration mode and drag reduction research in hypersonic flows using a counter-flow jet," *Chinese Journal of Theoretical and Applied Mechanics*, vol. 38, no. 4, pp. 438–445, 2006.

[57] E. Franquet, V. Perrier, S. Gibout, and P. Bruel, "Free underexpanded jets in a quiescent medium: a review," *Progress in Aerospace Sciences*, vol. 77, pp. 25–53, 2015.

[58] H. Chen, X. Li, X. Huang, and Z. Chen, "Aerodynamic heating reduction with jet array over leading edge of hypersonic vehicle," *Equipment Environmental Engineering*, vol. 15, no. 11, pp. 30–36, 2018.

[59] O. Peroomian, S. Chakravarthy, U. Goldberg, O. Peroomian, S. Chakravarthy, and U. Goldberg, "A 'grid-transparent' methodology for CFD," in *35th Aerospace Sciences Meeting and Exhibit*, p. 724, Reno, Nevada, USA, 1997.